EXPERIMENTAL INVESTIGATION OF THE HYDRODYNAMICS OF A PLUNGING TWO-PHASE PLANE JET

A Thesis
Presented to
The Academic Faculty

By

Brian Kern

In Partial Fulfillment
Of the Requirements for the Degree
Master of Science in Mechanical Engineering

Georgia Institute of Technology

August 2006

EXPERIMENTAL INVESTIGATION OF THE HYDRODYNAMICS OF A PLUNGING TWO-PHASE PLANE JET

Approved by:

Dr. Said Abdel-Khalik, Co-Advisor
College of Mechanical Engineering
Georgia Institute of Technology

Dr. S. Mostafa Ghiaasiaan, Co-Advisor
College of Mechanical Engineering
Georgia Institute of Technology

Dr. Sheldon Jeter
College of Mechanical Engineering
Georgia Institute of Technology

Date Approved: June 20, 2006

ACKNOWLEDGEMENTS

First and foremost, I would like to thank my co-advisors, Dr. Said Abdel-Khalik and Dr. S. Mostafa Ghiaasiaan. The thesis would not have been successful without their guidance, encouragement and support throughout the thesis project. I would also like to thank my thesis committee member Dr. Sheldon Jeter for his help.

I am also very grateful for the help I have received from Mr. Dennis Sadowski. In particular, his help with setting up lab equipment, modifying and designing components used in the experiment (i.e., the jet thickness tester), was essential to the thesis being completed in a timely manner.

I am very appreciative of the financial support I have received from Georgia Tech in the form of fellowships from Sandia and Southern Nuclear.

Lastly, I would like to thank my parents, Vince and Pam Kern, for their support of me throughout my life.

TABLE OF CONTENTS

LIST OF TABLES

LIST OF FIGURES

LIST OF SYMBOLS OR ABBREVIATIONS

A	Surface area (m^2), Activity (Ci)
C	Constant
$\dot{C}$	Collision rate per unit volume ($m^{-3}s^{-1}$)
CCD	Charge-coupled device
D	Diameter (m)
$\in$	Energy dissipation rate (J/s)
f	Friction factor
F	Force (N)
Fr	Froude number
g	Gravity (m/s^2)
G	Mass flux (kg/m^2-s)
H	Height (m)
I	Number of radiation counts
j	Superficial velocity (m/s)
k	Thermal conductivity (W/m-K)
$\dot{m}$	Mass flow rate (kg/s)
$\dot{N}$	Bubble number flux ($m^{-2}s^{-1}$)
p	Perimeter (m)
P	Pressure (Pa, psi)
ppm	Parts per million
Q	Volumetric flow rate (L/min, gpm)

r	Radius (m)
Re	Reynolds number
RMS	Root mean square
S	Slip ratio
t	Time (s)
T	Temperature (°C, K)
U	Velocity (m/s)
v	Specific volume (m^3/kg), Drift flux velocity (m/s)
V	Volume (m^3)
x	Position (m), Quality
w	Jet width (cm)
We	Weber number
$\overline{x}$	Average
z	Position (m)

Greek Letters

α	Void fraction, Alpha particle
β	Volumetric quality, Beta particle
γ	Gamma-ray
δ	Jet thickness (cm)
ε	Void fraction
λ	Decay constant (s^{-1})

μ	Dynamic viscosity (kg/m-s), Linear attenuation coefficient (m^{-1})
ν	Kinematic viscosity (m^2/s),
ρ	Density (kg/m^3)
σ	Surface tension (N/m), Standard deviation
τ	Stress (Pa)
ϕ	Two-phase friction factor multiplier

Subscripts

c	Continuous
CLT	Collapsed liquid thickness
Cr	Critical
d	Discontinuous
dr	Drainage
g	Gas
h	Homogeneous
i	Initial
in	Inlet
j	Jet
l	Liquid
lo	Liquid only
m	Mean

max	Maximum
MT	Measured thickness
rel	Relative
T	Transition
TP	Two-phase
Tu	Turbulent
VM	Virtual mass
w	Wall

SUMMARY

The hydrodynamics of falling two-phase jets were investigated. Experiments were performed using air and water. The jets were produced by injecting well mixed air-water mixtures through a 10 cm x 1 cm rectangular nozzle. The jet thickness and thickness-average void fractions were measured at nine different locations at three distances from the nozzle exit, and at three lateral locations for each specific distance from the nozzle for a total of 20 flow conditions. High speed photography and a needle tester were used for the measurements of the jet width and thickness respectively, and gamma-ray densitometry was applied for the void fraction measurement. Based on the experimental results, the two-phase jet stability was studied, and the void fractions were empirically correlated. Three different correlations were developed in order to provide flexibility with respect to their application. The correlations are of the generic form:

$$\frac{\varepsilon_g}{\varepsilon_{go}} = C_o Re_l^a Fr_l^b We_l^c D^{*d} \quad \text{(P.1)}$$

where ε_g is the local void fraction, ε_{go} is the homogeneous void fraction at the nozzle exit; Re_l, We_l and Fr_l are appropriately defined Reynolds, Weber and Froude numbers, and D^* is a ratio of lengths.

CHAPTER I

INTRODUCTION

I.1. MOTIVATION OF THESIS

A Z-Pinch reactor is a type of fusion power reactor. It operates by using pulsed power to compress and heat a D-T target to fusion conditions. The characteristics of this reactor are a high target yield (approximately 10 GJ) and a low repetition rate (approximately 0.1 Hz). The reactor generates X-rays, ions and neutrons and these particles can damage the cavity walls if they are not properly shielded. Liquid jets (Lithium-lead or Flibe) are used in order to protect cavity walls from the aforementioned radiation. The liquid jets will attenuate radiation, which will increase the lifetime of the cavity walls. However, the shock waves produced from rapidly heating and evaporating the liquid jets are difficult to contain within the small confines of the reactor cavity, which is due to the near incompressibility of the liquid. One solution to this problem is to use a two-phase, gas-liquid (Helium and lithium-lead or Flibe) jet. The compressibility of the two-phase jet allows for attenuation of the shock waves while still providing a means of protection for the cavity walls from the radiation. The high operating pressure of the Z-Pinch IFE reactor (approximately 20 torr) allows for introduction of the gas into the flow without excessively increasing the pumping requirements.

It is important to understand the hydrodynamic phenomena of two-phase flow. There are many different models of two-phase flow with varying assumptions and some

are analytic, semi-analytic, or empirical. The geometry and orientation of the flow precludes most empirical existing models from being used unless the specific geometry and orientation of the jet has already been studied. There is a scarcity of investigations regarding two-phase, downward flowing, free jets.

The objective of this work was to investigate the hydrodynamic behavior of downward-flowing plane two-phase flow jets. The jet stability and the evolution of void fraction along the jet were of primary interest as well as assessing the applicability of simple two-phase flow models.

The outline of the remainder of the thesis is as follows. In Chapter 2, the literature and theoretical background relevant to the two-phase jets are reviewed and discussed. In Chapter 3, the experimental setup and procedures are listed. In Chapter 4, the data analysis and results from the experiment are discussed. In Chapter 5, conclusions and recommendations are made based on the experimental results.

CHAPTER II

LITERATURE REVIEW AND THEORY

II.1. INTRODUCTION

Understanding the characteristics of two-phase flow is essential before two-phase jets can be discussed. In this chapter, first the many different flow regimes of two-phase flow are described and the transitions between the regimes are discussed. Several different two-phase models are then described and their capabilities for predicting various flow parameters such as void fraction are compared. Next, recent experiments of two-phase flow in various geometries are described and the resulting empirical correlations and results are discussed. Lastly, basic nuclear physics theory relevant to the application of the gamma-ray densitometer is conferred.

The fundamentals as well as the traditional applications of gas-liquid two-phase flow have been compiled and discussed in several textbooks and monographs. Among them, the books by Wallis (1969); Lahey and Moody (1993); and Collier and Thome (1994) are excellent sources.

II.2. FLOW REGIMES

Single phase flow has only three major flow regimes: laminar, transition, and turbulent flow. There are many different flow regimes in two-phase flow, however. It is

of great importance to determine the flow regime in most applications. The simplest method to determine the flow regime is by visual inspection. The sequence of flow regimes when the liquid flow rate is kept constant with a gas flow rate that increases is as follows. The first flow regime in a vertical co-current flow is bubbly flow. Bubbly flow is characterized by the gas phase distributed as bubbles within the liquid phase. The bubbles can vary in size from small and spherical to elongated with a spherical cap geometry. As the bubbles elongate further, the bubbles coalesce more and more, and the flow regime becomes slug flow. In the slug flow regime, the long, bullet shaped bubbles are separated from one-another by liquid slugs, and are separated from the pipe walls by a liquid film. As the gas flow increases, the slugs breakdown and the flow eventually becomes chaotic, and is dubbed churn flow. The flow field is churning in this regime, and it has a time-dependent character. As the gas flow increases, the flow regime switches to wispy-annular, which is characterized by a semi-continuous gas phase in the core of the flow field with entrained liquid droplets, and a liquid film phase that flows on the walls. Lastly, with increasing gas flow, the gas core becomes continuous and is surrounded by a thin liquid film on the wall, and is known as annular flow.

It is of great importance to understand the transition points between the flow regimes. This is usually done by using empirical flow regime maps. A good example is the widely used vertical flow pattern map developed by Hewitt and Roberts (1969). Their map is displayed in Figure. 2.1. Numerous other flow regime maps also exist, which apply to vertical and horizontal channels, rod bundles, etc.

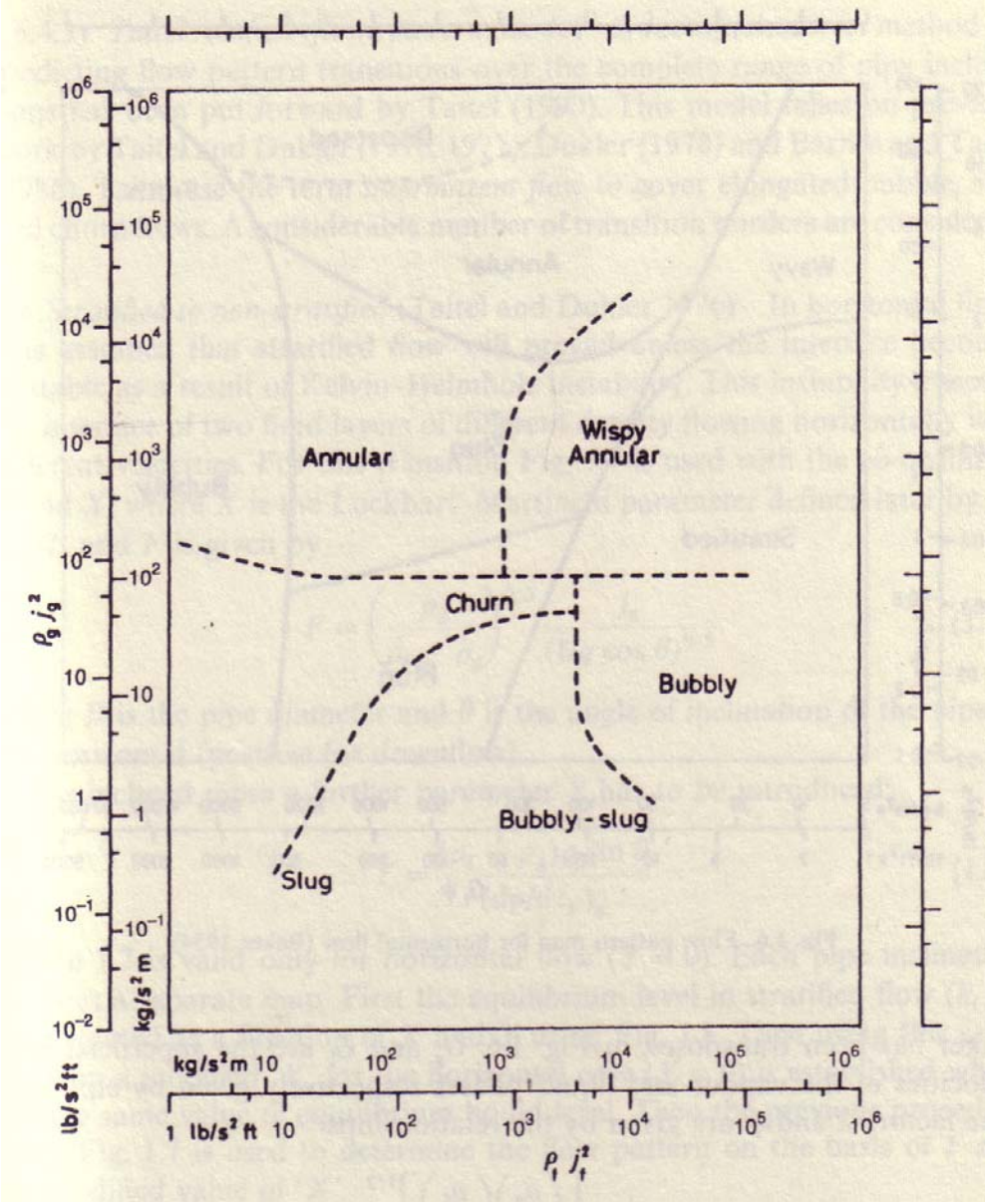

Figure 2.1 Flow regime map

II.3. TWO-PHASE MODELS

There are many different models for two-phase flow, which lead to tractable conservation and transport equations for two-phase flow, and can be used for the calculation of various parameters including the void fraction and pressure drop. Each

model varies in complexity depending on its foundation assumptions. The two chief assumptions are based on thermodynamic equilibrium and the relative velocities of the phases. By rearranging the most basic equations

$$\alpha = \frac{A_g}{A}, \quad (2.1)$$

$$\beta = \frac{\dot{Q}_g}{\dot{Q}_g + \dot{Q}_l}, \quad (2.2)$$

and

$$x = \frac{\dot{m}_g}{\dot{m}_g + \dot{m}_l}, \quad (2.3)$$

the void fraction can be shown as:

$$\alpha = \frac{1}{1 + \frac{1-x}{x}\frac{\rho_g}{\rho_l}S} \quad (2.4)$$

where S is the slip ratio, which is the ratio of the gas to liquid velocities,

$$S = \frac{U_g}{U_l}. \quad (2.5)$$

II.3.1. Homogeneous Equilibrium Model

The simplest model is the homogenous equilibrium model (HEM). The assumptions of the HEM are that the gas and liquid velocities are equal so only one momentum equation is needed (the slip ratio is 1); the two phases are in thermodynamic equilibrium; and the single phase friction factor concept can be used for the two-phase flow, provided that appropriate two-phase flow properties are defined and used. Equation

2.4 is useful determining the void fraction, and the following is used for the homogeneous flow density:

$$\bar{\rho} = \rho_h = \frac{G}{j} = \alpha\rho_g + (1-\alpha)\rho_l = \left[v_l + x(v_g - v_l) \right]^{-1}. \quad (2.6)$$

The HEM model can be easily used for determining the pressure gradient. The differential wall shear force can be written in terms of shear stress

$$d\bar{F} = \tau_W \, p dz \quad (2.7)$$

and the wall shear stress as

$$\tau_W = f_{TP} \left(\frac{\bar{\rho}\bar{U}^2}{2} \right) \quad (2.8)$$

where f_{TP} can be formed from an appropriate friction factor such as the Blasius correlation

$$f_{TP} = 0.079 \left[\frac{GD}{\bar{\mu}} \right]^{-1/4}. \quad (2.9)$$

Further one-dimensional analysis yields,

$$-\left(\frac{dP}{dz} F \right) = \frac{1}{A} \frac{d\bar{F}}{dz} = \frac{\tau_W \, p}{A} = \frac{f_{TP} \, p}{A} \left(\frac{\bar{\rho}\bar{U}^2}{2} \right). \quad (2.10)$$

Substituting for τ_W and using the definition of the Fanning friction factor, one gets:

$$-\left(\frac{dP}{dz} F \right) = \frac{2 f_{TP} G^2 \bar{v}}{D} = \frac{2 f_{TP} G j}{D}. \quad (2.11)$$

The acceleration pressure term can be expressed as

$$-\left(\frac{dP}{dz} a \right) = G^2 \frac{d}{dz} \left[\frac{x^2 v_g}{\alpha} + \frac{(1-x)^2 v_f}{(1-\alpha)} \right] = G \frac{d(\bar{U})}{dz} = G^2 \frac{d(\bar{v})}{dz} \quad (2.12)$$

where

$$\frac{d(\bar{v})}{dz} = v_{fg}\frac{dx}{dz} + x\frac{dv_g}{dP}\left(\frac{dP}{dz}\right), \quad (2.13)$$

and lastly the static head as

$$-\left(\frac{dP}{dz}z\right) = g\sin\theta\left[\alpha\rho_g + (1-\alpha)\rho_l\right] = \bar{\rho}g\sin\theta = \frac{g\sin\theta}{\bar{v}}. \quad (2.14)$$

And finally, the total pressure gradient is the sum of the frictional, acceleration, and static components (Collier and Thome, 1996)

$$-\left(\frac{dP}{dz}\right) = \frac{\dfrac{2f_{TP}G^2v_f}{D}\left[1+x\left(\dfrac{v_{fg}}{v_f}\right)\right] + G^2v_f\left(\dfrac{v_{fg}}{v_f}\right)\dfrac{dx}{dz} + \dfrac{g\sin\theta}{v_f\left[1+x\left(\dfrac{v_{fg}}{v_f}\right)\right]}}{1+G^2x\left(\dfrac{dv_g}{dP}\right)}. \quad (2.15)$$

The term for the average two-phase dynamic viscosity, $\bar{\mu}$, used in the Blasius correlation, can be expressed using the following relationships,

$$\frac{1}{\bar{\mu}} = \frac{x}{\mu_g} + \frac{(1-x)}{\mu_l} \quad (2.16)$$

(McAdams, 1942),

$$\bar{\mu} = x\mu_g + (1-x)\mu_l \quad (2.17)$$

(Cicchitti, 1960) and

$$\bar{\mu} = \bar{\rho}\left[xv_g\mu_g + (1-x)v_l\mu_l\right] \quad (2.18)$$

(Dukler, 1964). Furthermore, the friction term can be rewritten

$$-\left(\frac{dP}{dz}F\right) = -\left(\frac{dP}{dz}F\right)_{lo}\left[1+x\left(\frac{v_{fg}}{v_f}\right)\right]\left[1+x\left(\frac{\mu_{fg}}{\mu_g}\right)\right]^{-1/4}. \quad (2.19)$$

For simplicity one can use the concept of two-phase multiplier, and write

$$-\left(\frac{dP}{dz}F\right)=\phi_{lo}^{2}\left(-\frac{dP}{dz}F\right)_{lo} \quad (2.20)$$

and

$$\left[1+x\left(\frac{v_{fg}}{v_f}\right)\right]\left[1+x\left(\frac{\mu_{fg}}{\mu_g}\right)\right]^{-1/4}=\phi_{lo}^{2}. \quad (2.21)$$

The concept of the two-phase flow multiplier is quite general, however, and in practice values of ϕ_{lo}^{2} are measured and tabulated or correlated.

II.3.2. Separated Flow Model

The separated flow model treats the two phases as two separate streams, each moving at a different mean velocity. A mass and momentum conservation equation is derived for each respective phase, but the number of energy equations is either one or two depending on whether one of the phases can be assumed to be saturated.

The separated flow modeling technique evidently provides more detailed predictions about the behavior of the flow field. To apply this method one needs a large number of constitutive and closure relations, however. Closure relations are thus needed for phase-wall and phase-phase interactions and transport processes, many of which are poorly understood. An example of difficult closure relations is the virtual mass force, which is a basic force exchanged between two phases. The force appears if one of the phases is accelerating with respect to another, and shows up in analysis when the two-phase conservation equations are averaged. Exact analytical expressions for the virtual mass force term are only available for some simple and idealized flow configurations. For

example, the virtual mass force term acting on a sphere that moves through a quiescent fluid in the creep flow regime is (Clift, et al., 1978)

$$F_{VM} = \rho \frac{\pi D^3}{12} \frac{dU}{dt} \quad (2.22)$$

where ρ is the density of the fluid, D is sphere's diameter, and U is the velocity of the sphere. For more complicated flow situations, and in particular for widely-encountered two-phase flow regimes, simpler expressions are often used. An example is the following expression, derived by Ishii and Mishima (1984):

$$F_{VM} = \frac{1}{2} \alpha_d \frac{1+2\alpha_d}{1-\alpha_c} \rho_c \left[\frac{D_d \left(\vec{U}_d - \vec{U}_c \right)}{Dt} - \left(\vec{U}_d - \vec{U}_c \right) \bullet \nabla U_c \right] \quad (2.23)$$

where the virtual mass force, F_{VM}, is defined per unit mixture volume. The subscripts c and d refer to the continuous and discontinuous phases respectively. Also,

$$\frac{D_d}{Dt} = \frac{\partial}{\partial t} + \vec{U}_d \bullet \nabla \quad (2.24)$$

and it should be noted that the virtual mass term is only significant if the gas phase is dispersed and if the acceleration is extreme.

Empirical correlations are often used for various wall-fluid and gas-liquid interfacial phenomena, perhaps most importantly for the two-phase pressure drop multipliers such as ϕ_{lo}^2. There is no need for empirical correlations for α, however, since it is related to the phase velocities and flow quality according to the fundamental void-quality relations (Wallis, 1969; Lahey and Moody, 1993):

$$\alpha = \frac{x}{x + \frac{\rho_g U_g}{\rho_l U_l} (1-x)} \quad (2.25)$$

Note that the separated flow model predicts the phase velocities and the flow quality by solving the phase conservations equations. In summary, the flow regime dependency of most of the constitutive relations is a limitation of the model, and another drawback is the inaccuracy associated with the interfacial transport relations.

II.3.3. Slip Models and the Drift Flux Model

Diffusion models are based on solving only one momentum equation (usually a mixture momentum equation) while treating the two phases as separate streams. This is achieved by using an algebraic correlation in addition to the conservations equations that provides for the calculation for the velocity difference between the two phases.

A widely-used approach for diffusion modeling is to develop and apply a correlation for the slip ratio, defined as

$$S = \frac{U_g}{U_l} . \quad (2.26)$$

The most important and widely-used diffusion model is the drift flux model.

The drift flux model is thus a semi-empirical diffusion model that provides understanding of phase velocity ratio (slip ratio) and does so using two empirically adjusted parameters. The model's assumptions include that the flow is in steady-state and negligible wall shear stress. The model is only valid for one-dimensional flow. Consider the flow field shown in Figure 2.2

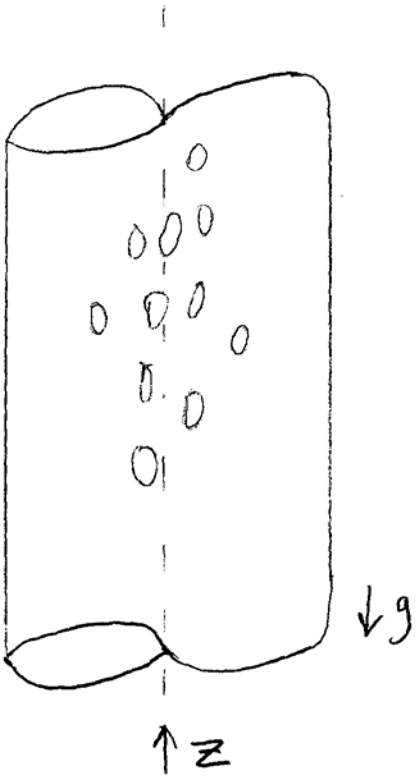

Figure 2.2 Flow field for drift flux analysis

The total volumetric flux j is defined as the sum of superficial velocities of the liquid and gas components,

$$j = j_g + j_l = \frac{Q_g + Q_l}{A}. \quad (2.27)$$

Using the definition of the volumetric flux, the gas superficial velocity can be found by multiplying the following identity relation with α:

$$U_g = j + \left(U_g - j\right) \quad (2.28)$$

and the result would be:

$$j_g = \alpha j + \alpha\left(U_g - j\right). \quad (2.29)$$

Two drift flux parameters are then defined using area-averaged terms,

$$C_0 = \frac{\langle \alpha j \rangle}{\langle \alpha \rangle \langle j \rangle} \quad (2.30)$$

and

$$V_{gj} = \frac{\langle \alpha (U_g - j) \rangle}{\langle \alpha \rangle}. \quad (2.31)$$

By expressing the superficial phasic velocities in terms of the quality,

$$j_g = \frac{Gx}{\rho_g} \quad (2.32)$$

and

$$j_l = \frac{G(1-x)}{\rho_l} \quad (2.33)$$

and using the aforementioned parameters, the following void fraction-quality relation can be derived.

$$\alpha = \frac{x}{C_0 \left[x + \frac{\rho_g}{\rho_l}(1-x) \right] + \frac{\rho_g V_{gj}}{G}}. \quad (2.34)$$

The above equation is now a closure relation that replaces a phase momentum equation. The drift flux method is useful as a stand-alone correlation, however. Using empirical correlations for the drift flux parameters C_0 and V_{gj} one can calculate the void fraction. The empirical correlations are flow regime dependent, however, and the model is most accurate for bubbly, slug, and churn flow. Knowing C_0 and V_{gj}, the slip ratio can be calculated from:

$$S = C_0 \frac{x(C_0 - 1)\rho_l}{\rho_g (1-x)} + \frac{\rho_l V_{gj}}{G(1-x)} . \quad (2.35)$$

One of the founders of the drift flux model was Zuber (see Zuber and Findlay, 1965). The investigation of Zuber and Findlay is now briefly discussed.

Zuber and Findlay (1965) developed a two-dimensional drift flux model to account for changes in flow parameters across the flow area, which extended the one-dimensional model developed by Wallis (1962). Accordingly they wrote,

$$\frac{j_g}{\alpha} = C_0 j + v_g^{'} \quad (2.36)$$

where

$$C_0 = \frac{\frac{1}{A}\int_A \alpha j dA}{\left(\frac{1}{A}\int_A \alpha dA\right)\left(\frac{1}{A}\int_A j dA\right)} \quad (2.37)$$

and

$$v_g^{'} = v_g - j . \quad (2.38)$$

Zuber and Findlay attempted to predict the value of C_0 based on known velocity and void profiles, and their conclusions are the following:

1. The value of C_0 depends on the flow and concentration profiles.
2. For fully established profiles in axi-symmetrical two-phase flow, C_0 may range from 1.0 to 1.5 when the gas phase has a higher concentration in the center of the flow than the walls.

3. When the gas phase is concentrated near the wall, as for example, during subcooled boiling, C_0 can have a value of less than unity.

4. For fully established and constant profiles, the value of C_0 is constant.

Comparing the volumetric flux with the ratio of the gas component of the flux to the gas void fraction, a flow regime map was made, and it defined the transition between bubbly and churn-turbulent flow. The dependence of C_0 on Re_l in bubbly flow is plotted, and it is noted that the dependence changes when $Re_l \approx 4000$ - approximately the transition from laminar to turbulent flow (see Figure 2.3). As the flow becomes highly turbulent, C_0 approaches a constant value. A plot was made for churn-turbulent flow as well (see Figure 2.4), and while a similar contour was noted, the values of C_0 were lower.

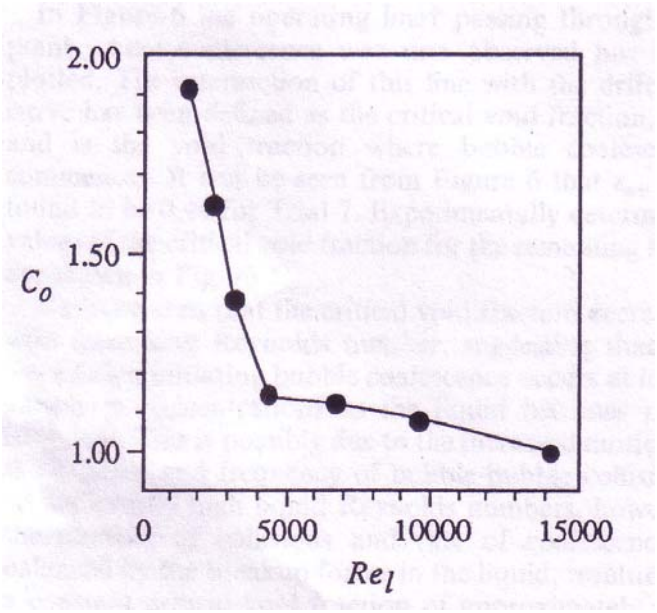

Figure 2.3 C_0 **vs** Re_l **for the bubbly flow regime**

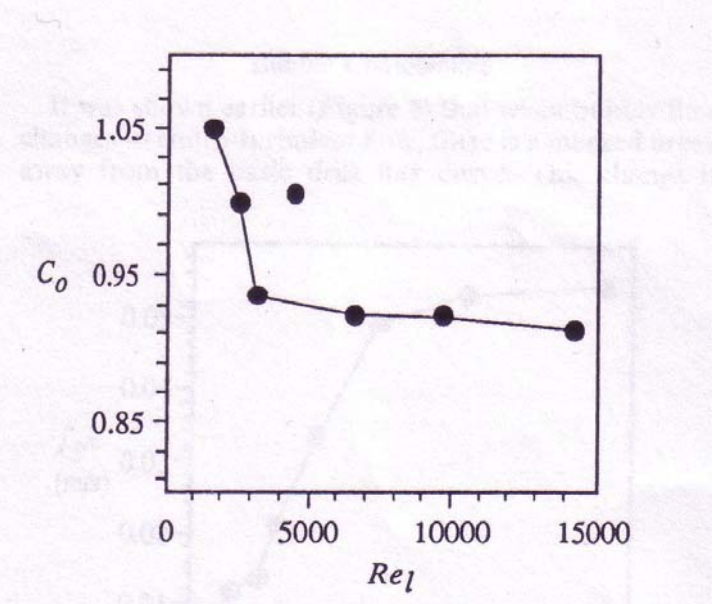

Figure 2.4 C_0 **vs** Re_l **for the churn-turbulent regime**

For various values of Re_l, the critical gas void fraction was measured above which bubbly flow would not be sustainable. As the liquid Reynolds number increased, the critical gas void fraction decreased. When the flow becomes turbulent, the critical gas void fraction approaches a constant value of 0.24. An explanation for this phenomenon is that the mechanism that initiates bubble coalescence occurs at lower gas concentrations as the flow becomes more turbulent. While the bubble size remains relatively constant in the bubbly flow regime in common pipe flow, when the flow transitions to churn-turbulent flow, the bubble size increases. For each bubble size a new drift-flux curve would need to be drawn. Once the liquid Reynolds number is sufficiently large (10,000), the value of j_g' / α approaches a constant value $(0.055 m/s)$ where

$$j_g^{'} = \alpha v_g^{'} \quad (2.39)$$

This indicates a possible equilibrium between bubble breakup and coalescence (Evans and Jameson, 1995).

Empirical correlations for C_0 and V_{gj} for various flow configurations and conditions are available. A widely used expression for churn-turbulent flow regime, for example, is (Zuber et al., 1967)

$$V_{gj} = 1.41\left[\sigma g\left(\rho_l - \rho_g\right)/\rho_l^2\right]^{1/4}. \quad (2.40)$$

The following simple representation also agrees with slug flow data quite well (Nicklin et al., 1962):

$$C_0 = 1.2\,;\; V_{gj} = 0.35\sqrt{gD\left(\rho_l - \rho_g\right)/\rho_l} \quad (2.41)$$

the right side of the latter equation in fact represents the rise velocity of Taylor bubbles in stagnant liquid (Davidson and Harrison, 1971).

II.4. FLOW PHENOMENA IN TWO-PHASE FALLING JETS

A brief discussion of the hydrodynamic phenomena in falling and plunging two-phase jets will be presented in this chapter.

Plunging jets are encountered in plunging bubble columns. Bubble columns are chemical reactors that provide for mass transfer between a gas and liquid stream. Conventional bubble columns operate in countercurrent mode (downward liquid flow and upward moving gas). An important flow limitation for conventional bubble columns is that the downward liquid velocity must be smaller than the rise velocity of the gas bubbles, otherwise unfavorable flow regimes develop in the column. Plunging jet bubble

columns are meant to remedy this limitation by operating in cocurrent (downward) flow configuration. Figure 2.5 is a schematic of a plunging jet bubble column. As noted, the column includes a free liquid jet zone where a downward-moving two-phase jet occurs, followed by a pipe flow zone. The two-phase flow in this system, in particular in the free jet zone, is somewhat similar to a falling two-phase jet. An example of an experimental setup that is designed to produce bubble columns is shown in Figure 2.6.

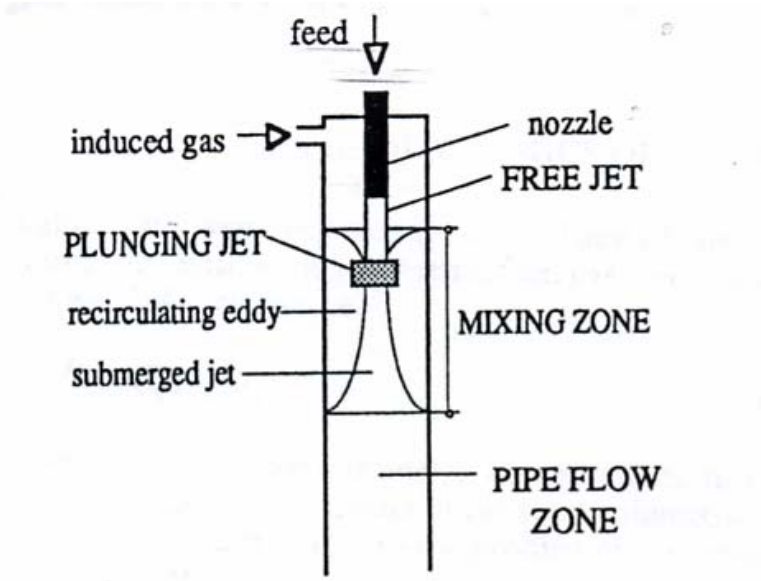

Figure 2.5 Plunging liquid jet bubble column showing different hydrodynamic regions

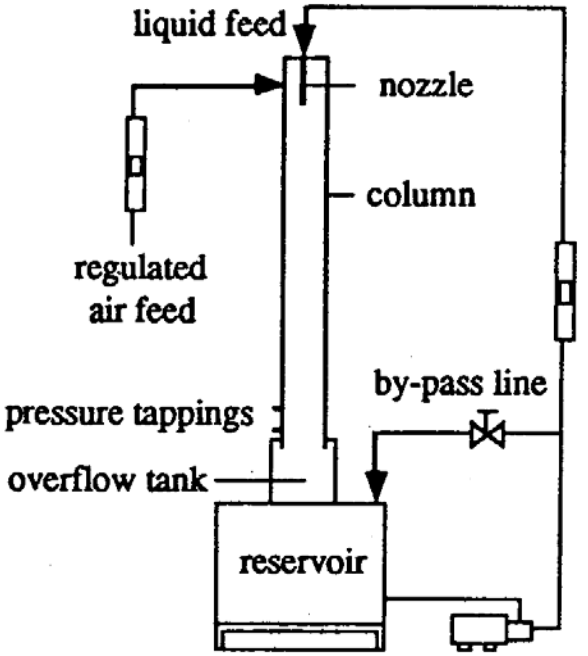

Figure 2.6 Experimental apparatus for producing a bubble column

(Evans and Jameson, 1995)

Downward flowing gas-liquid two-phase mixtures are encountered in plunging jet bubble columns. A schematic of a typical plunging jet bubble column is displayed in Figure 2.5. The hydrodynamic processes that determine the operating characteristics of a plunging jet bubble column take place in four regions within the column. The first region is the free jet zone, which is a region between the nozzle and the free surface of the bubbly mixture. The second region is the plunging jet zone, which is the region where the falling jet penetrates the bubbly mixture. The third region is the mixing zone, which is the region that spans from the submerged jet just below the point where it plunges into the fluid recirculating at the column's top. The fourth region is the pipe-flow zone, which is the region that is below the mixing zone. For most applications of a plunging liquid jet, the flow regime desired in the pipe-flow zone is bubbly flow. Bubbly flow has

advantageous characteristics, most notably its stability and its large interfacial area. As the gas flow rate increases, the flow regime changes to churn-turbulent flow. Churn-turbulent flow has detriments that include a relatively small interfacial area as well as large bubbles that may coalesce and rise within the column, preventing additional gas flow. From the view point of plunging jet bubble columns, it is therefore pertinent to study the hydrodynamic mechanisms and the flow conditions that transform the flow from bubbly to churn-turbulent (Evans and Jameson, 1995).

II.4.1. Gas Entrainment

As mentioned above, in the plunging bubble columns, the liquid is flown downwards (through various geometries) and gas is introduced into the liquid typically by means of a porous tube. The liquid carries the gas bubbles from the tubing, downwards through the column. Previous studies have shown that when the liquid velocity is small, the gas bubbles coalesced and the gas-liquid flow became unstable. When the drag force is unable to overcome the gas buoyancy forces, the jet may shatter. Once the velocity of the liquid is large enough, the system will stabilize as cocurrent flow and operate with a large throughput. An experimental study by Yamagiwa et al. (1990) showed that as the liquid velocity increased, the two-phase flow went through several flow regimes. Their reported regimes are shown in Figure 2.7: bubble stagnant flow (A), non-uniform bubbling flow (B), uniform bubble flow (C), churn-turbulent flow (D), and again uniform bubble flow (E).

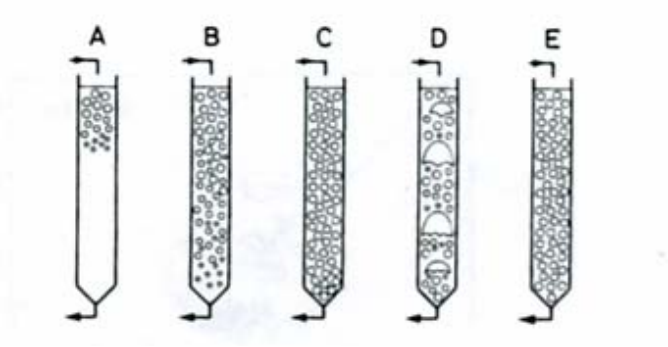

Figure 2.7 Flow regimes observed in a bubble column

An interesting result was that the flow digressed and then regressed back to the same uniform bubbly flow regime. In the case of the high liquid velocity bubble flow regime, the bubbles flowed downward without coalescence. In addition, gas was entrained from the ambient air by the downward-flowing jet. The gas entrainment rate was measured. The authors then compared their results with prior experiments for consistency. The transition from bubbly to churn flow is very important in bubble columns because in the churn-turbulent regime, the interfacial surface area concentration is considerable lower than in bubbly flow. The transition thus leads to the deterioration of the column performance. Using their experimental results, Yamagiwa et al. were able to empirically correlate the velocity for regime transition from churn-turbulent flow to uniform bubbly flow, according to:

$$Fr_T^{0.91} Re_T^{0.09} = 0.246(D_c / D_n)^{0.21}(L_j / D_n)^{0.16}(H_f / D_c)^{0.43} \quad (2.42)$$

where Fr_T and Re_T correspond to the transition liquid velocity U_{IT}. When rewritten in terms of U_{IT}, the above equation gives:

$$U_{IT} = 2.00 \times 10^{-1} D_C^{0.05} D_n^{-0.28} L_j^{0.16} H_f^{0.43}. \quad (2.43)$$

These equations are valid for the following geometric and flow parameters:

Table 2.1 Parameter ranges in the experiment by Yamagiwa et al. (1990)

D_n[m]:	0.008, 0.010, 0.011, 0.013, 0.015, 0.018, 0.020
L_j[m]:	0.030, 0.060, 0.090, 0.150
D_c[m]:	0.034, 0.050, 0.060, 0.070
H_f[m]:	1.20, 1.50, 1.80, 2.00
Q_l[m^3/s]:	3.17 x 10^{-4} – 2.00 x 10^{-3}

As mentioned, the regime transition from bubbly flow to churn flow is particularly important since the interfacial area and gas throughput are large in the uniform bubble regime and the flow is stable.

The effect of the fluid properties on gas holdup was also studied by Yamagiwa et al. (1990). Based on their experimental data, the following empirical correlations were developed for the gas holdup, as well as for the gas entrainment rate:

$$U_g / \varepsilon_g = 1.17 \times (U_g + U_l) - 0.19 \quad (2.44)$$

and

$$Q_g / Q_l = 2.24 \times 10^{-3} Fr^{0.40} Re^{0.26} (L_j / D_n)^{0.48}. \quad (2.45)$$

It was also found that the energy needed for the injection of gas was smaller, in comparison with conventional columns in this configuration. This supports the usefulness of this aeration technique in industry as it is both efficient and capable of handling large quantities of gas.

In an earlier study conducted by Ohkawa et al. (1985), the characteristics of downward bubble columns were investigated. It was determined from this study that ε_g depended on V_j and L_j. Interestingly however, the nozzle diameter had little effect. They correlated their data according to:

$$\varepsilon_g = 3.96\times10^{-1} V_j^{0.78} L_j^{0.38}, \quad (2.46)$$

The above correlation is in terms of the jet velocity at nozzle exit, V_j. It can be cast in terms of the liquid superficial velocity, U_j, within 10% error to derive:

$$\varepsilon_g = 3.96\times10^{-1} U_j^{0.78} \left(D_n / D_c\right)^{-1.56} L_j^{0.38}. \quad (2.47)$$

The range of parameters for the validity of the above correlations can be found in Table 2.2.

Table 2.2 Flow parameters in the experiments by Ohkawa et al. (1985)

$D_t \times 10^2$ [m]	$D_n \times 10^2$ [m]	$L_j \times 10^2$ [m]	$U_l \times 10^2$* [m/s]	V_j** [m/s]	Keys
		3	14.9–17.2	2.21–2.54	◆
	1.3	6	13.9–15.5	2.06–2.29	◆
		9	13.4–14.6	1.98–2.15	◆
5.0					
		3	15.9–18.9	1.77–2.11	◇
	1.5	6	14.9–17.1	1.65–1.90	◆
		9	14.3–16.1	1.59–1.79	◆
		3	14.5–16.0	2.33–2.56	▬
	1.5	6	13.6–14.4	2.17–2.31	▬
		9	13.0–13.6	2.08–2.17	◪
		3	15.8–18.2	1.75–2.02	■
6.0	1.8	6	14.7–16.4	1.64–1.82	◨
		9	14.1–15.4	1.57–1.71	◧
		3	16.5–19.5	1.49–1.76	□
	2.0	6	15.4–17.6	1.39–1.59	◫
		9	14.8–16.6	1.33–1.49	⊟
		3	14.6–15.8	2.21–2.38	⊘
	1.8	6	13.6–14.2	2.06–2.15	◔
		9	13.1–13.4	1 98–2.02	◑
		3	15.3–17.0	1.88–2.08	◒
	2.0	6	14.3–15.3	1.75–1.87	◓
		9	13.7–14.4	1.68–1.76	⊘
7.0					
		3	16.0–18.1	1.62–1.83	●
	2.2	6	14.9–16.3	1.51–1.65	◑
		9	14.3–15.4	1.45–1.55	◐
		3	16.9–20.0	1.33–1.55	○
	2.5	6	15.8–17.8	1.24–1.40	⊕
		9	15.2–16.8	1.19–1.32	⊖

The correlation was then plotted against the measured void fraction.

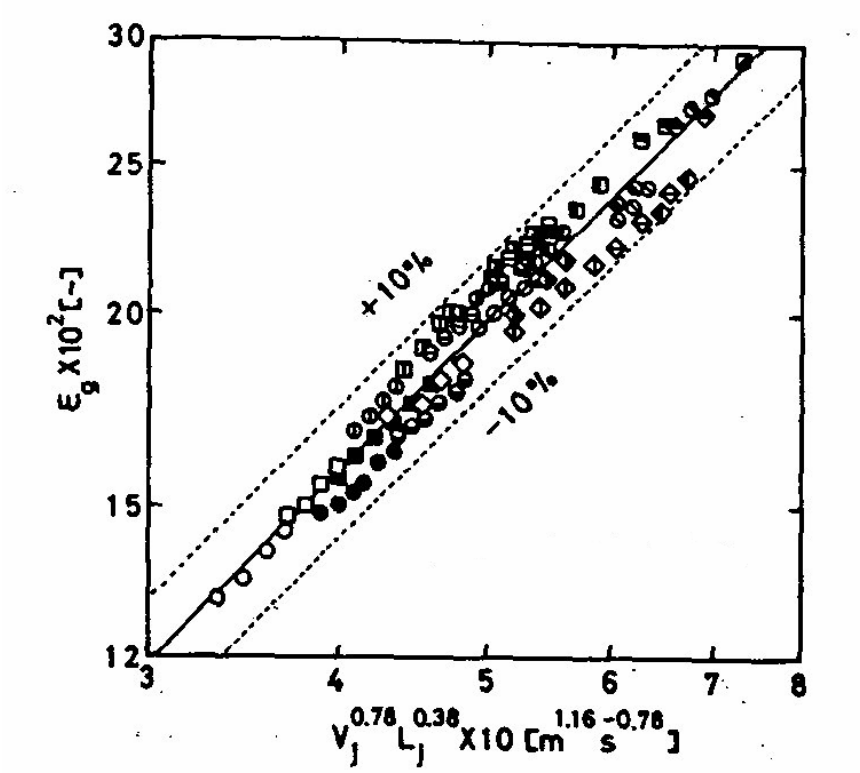

Figure 2.8 Relationship between ε_g and $V_j^{0.78} L_j^{0.38}$

II.4.2. Bubble Behavior

The behavior of bubbles in turbulent two-phase jets has been studied by several investigations, including Kumar et al. (1989) and Stanley and Nikitopoulos (1996). Much attention has been paid to the effect of bubbles on the turbulence in the liquid jet.

In the experiment conducted by Stanley and Nikitopoulos (1996), a one component Phase-Doppler Velocimetry system (a non-intrusive technique involving light-scattering) was used to measure the bubble size and velocity, in water-air falling jets, and the exit dimension of the jet is 12.7 mm in diameter. The nozzle of the jet was designed using a cubic contour, which provided a “top-hat” profile at the jet exit and the

turbulence at the jet's exit was minimal (approximately 2%) (Morel, 1975). The first study investigated two bubble related properties – the size of the bubbles and their size distribution. These were measured against the average and RMS fluctuation velocities of the bubbles in the developing and fully developed jet regions. The experiments were run at a fixed Reynolds number (11,565) and three different gas injection assemblies. The different gas injection assemblies were used to vary the initial bubble conditions (size and distribution). The gas volume fraction at the inlet used in the experiments was low (0.47%). To ensure the homogeneity within the two-phase flow, air was injected into the flow eight jet diameters upstream from the nozzle exit via a stainless steel porous tube.

The Phase-Doppler Velocimetry method measures the liquid velocity as well as the bubble velocity and size using light-scattering. The velocity of the bubble crossing the probe volume (the intersection of two beams) is calculated from the Doppler frequency shift of the scattered light (Durst et al., 1976). And the scatterer's size is proportional to the phase difference, where the proportionality constant depends on parameters such as the incident light wavelength, the angle between incident beams, and the photo-detector position and orientation (Durst and Zare, 1975). The light scattering system used by Stanley and Nikitopoulos (1996) was a Spectra-Physics 2000 series argon-ion laser, a fiber optic transmitting cable, transmitting and receiving optics, photomultipliers, and a signal processing unit. Image processing equipment was also used (CCD camera).

An incentive for the investigation of Stanley and Nikitopoulos (1996) was that the previous studies had shown contradictory trends with respect to the effect of gas flow rate on the axial and radial turbulence intensity variation in two-phase jets as well as pipe flows. The cause of the contradictory trends is believed to be the effect of the bubble size,

which in turbulent flow is loosely determined by injection conditions and bulk flow conditions. Moreover, experiments have also shown that there may be lower and upper limits to bubble sizes in turbulent flow conditions.

The results of the experiments of Stanley and Nikitopoulos (1996) show that the bubble size and size distribution along with other bubble exit conditions (i.e., at exit from the nozzle where the jet originates) can influence the RMS velocity fluctuations of the bubbles especially in the jet development region. However, the average bubble velocities are not very sensitive to initial and exit bubble conditions. In two of the three cases that these authors studied, bubbles were ejected laterally by the exit of the jet due to the large velocity gradient created by the axisymmetric shear layer. This was more proof that the initial jet conditions affect the jet's exit flow.

An earlier study conducted by Kumar et al. (1989) addressed the effects of bubbles on the turbulence levels of a jet. A falling liquid jet was mixed with air inside a tank. Air was injected into the liquid jet via needles, and images were taken using a method similar to the experiment of Stanley and Nikitopoulos (1996). The results from the experiment clearly showed that turbulence levels within the jet are increased with the addition of bubbles. Furthermore, at low Reynolds numbers, the addition of bubbles changed the geometry of the jet by increasing the jet width, and the changes were most significant near the exit of the jet.

II.4.3. Bubble Size Distribution

The investigation of the size distribution of bubbles in two-phase flow is essential for understanding the behavior of plunging liquid jet bubble columns. In the experiment conducted by Atkinson et al. (2003), a plunging liquid jet bubble column was studied. The flow consisted of water (136 L/min) and air (41 L/min); methylisobutylcarbinol (MIBC® 20 ppm) was added to the system to reduce bubble coalescence. A camera was used to gather information, and the images were analyzed using BioScan Optimas software.

Atkinson et al. compared various size distribution models with their experimental data in order to study bubble breakup and coalescence behavior. The size distribution model used by Atkinson et al. (2003) is based on the bubble number flux balance over a unit volume:

$$\dot{N}(z_2) = \dot{N}(z_1) - \int_{z_1}^{z_2} P_C \dot{C}(z) dz \quad (2.48)$$

where $\dot{C}(z)$ is the collision rate per unit volume and P_C is the probability that a collision occurring between two bubbles will cause a coalescence event. The probability depends on the ratio of drainage and interaction times, which is defined as

$$\frac{t_{dr}}{t_i} = \frac{k}{2\pi}\left(\frac{3\rho_L \mu_{rel} d}{C_{VM}\sigma}\right)^{1/2} \quad (2.49)$$

where C_{VM} is the virtual mass coefficient, k is a correction factor, and μ_{rel} is the relative velocity of the two bubbles. The drainage time is related to the drainage of the liquid that separates the two colliding bubbles. The liquid turns into a tenacious film as the bubbles

approach, and must be drained before coalescence can materialize. Once this ratio is obtained, the probability is

$$P_C \approx \exp(-t_{dr} / t_i)\,. \quad (2.50)$$

The collision rate per unit volume is defined as (Kuboi et al., 1972),

$$\dot{C} = \left(\frac{8\pi}{3}\right)^{1/2} n(z)^2 d(z)^2 v_T(z) \quad (2.51)$$

where $n(z)$ is the bubble number density and $v_T(z)$ is the turbulent velocity scale. If the bubbles are spherical, the bubble number density can be represented as

$$n(z) = \frac{6 \in (z)}{\pi d(z)_{VS}^3}\,. \quad (2.52)$$

The turbulent velocity scale is obtained based on the behavior of inertial eddies in a locally isotropic turbulent field (Hinze, 1975):

$$v_{Tu}(z) = \left(\frac{\in (z) d(z)}{\rho_L}\right)^{1/3} \quad (2.53)$$

where $\in (z)$ represents the turbulent energy dissipation rate.

By applying the Weber number (a ratio of inertia to surface tension forces) and analyzing flow properties in the mixing zone, the maximum bubble size can be determined for which the system will remain stable. Moreover by relating the critical Weber number (the value of We_{cr} was assumed to be equal to 1.2) to the average energy dissipation rate per unit volume, $\in$, an expression for the maximum bubble diameter was derived from

$$D_{max} = (We_C \sigma / 2)^{3/5} (\rho_L)^{-1/5} (\overline{\in})^{-2/5} \quad (2.54)$$

(Evans et al., 1992).

It was also shown by Atkinson et al. (2003) that the energy dissipation rate in the flow zone was much lower than the dissipation rate in the mixing zone. Since little energy was being dissipated in the flow zone, there was not much bubble breakup. The bubble coalescence rate was defined as

$$\dot{N}(z) = \frac{24 Q_g}{\pi^2 d_V(z)^3 D_C^2}. \quad (2.55)$$

Another interesting conclusion from the study by Atkinson et al. (2003) was that bubble coalescence in the column is a binary process. Physically this means that each coalescent event decreases the number of bubbles by one, as opposed to simultaneous coalescence of bubble clusters. The experiment also tested the effectiveness of a surfactant that sought to reduce the collision probability among the bubbles. When the surfactant MIBC® was used, it increased the bubble persistence time (lifetime) by an order of magnitude.

II.5. GAMMA-RAY DENSITOMETER

II.5.1. Basic Nuclear Theory

In order to understand a key component of the experiment, the gamma-ray densitometer, it is beneficial to understand the governing nuclear principles. The nuclear structure of an atom consists of a mixture of neutrons and protons. The number of protons defines the element, and the number of neutrons defines the isotope of the specified element. When the number of neutrons becomes either too small or too large, the nucleus becomes unstable. Unstable nuclei will undergo radioactive decay in order to become

stable. If the nucleus has an excess of neutrons, the decay can be in the form of β^- decay, which is an emission of an electron and an antineutrino. In other cases, the decay can be in the form of β^+ decay or electron capture. The former is an emission of a positron and a neutrino, and the latter is where interaction with a nearby nucleus yields an additional neutron at the expense of an electron and proton. The electron vacancy is then filled by another electron. Another type of decay is α decay. An α particle is a Helium-4 nucleus and consists of two protons and two neutrons; and, it is much heavier than the previously mentioned β particles.

The nucleons (neutrons and protons) that comprise a nucleus have a ground state. At their ground state, the nucleons are in their lowest state of energy. The daughter nucleus formed from the aforementioned nuclear decay is often left in an excited state. In order to reach a ground state, the nucleus undergoes γ decay. The energy of the gamma-ray is simply the energy difference between the excited and ground states of the nucleus.

It is desirable to determine the decay rate (activity) of a material, which is modeled by a differential equation,

$$A = \lambda N = -\frac{dN}{dt} \quad (2.56)$$

where N is the number of atoms present and λ is the decay constant. The decay constant of a material is inversely proportional to its half-life. Solving the differential equation yields

$$A = A_0 e^{-\lambda t} \quad (2.57)$$

where A_0 is the activity at $t = 0$.

Now that the sources of gamma-rays and the exponential nature of radioactive decay are clear, it is important to understand their interactions with matter. For a beam of gamma-rays traveling in the x-direction into a slab of some material, analogous to radioactive decay, the governing differential equation is

$$dN = -\mu N dx \quad (2.58)$$

where μ is the linear attenuation coefficient, and the solution yields

$$N = N_0 e^{-\mu x} \quad (2.59)$$

where N_0 is the initial amount of gamma-rays that entered the slab. The linear attenuation coefficient depends on the material of the slab as well as the kinetic energy of the gamma-rays. It is important to note that if the beam of radiation is tightly collimated, any form of interaction of the gamma-ray with the slab will cause scattering. Therefore, a radiation detector placed directly on the other side of the beam will only record the number of gamma-rays that did not interact with the medium.

II.5.2. Statistical Error Analysis

If two different types of slab materials are used, and the gamma-rays are kept at a fixed energy (mono-energetic), the difference in the number of gamma-particles detected can be solely attributed to the type of slab material. Therefore, in the case of this experiment, measurements can be taken with the desired flow as the medium and repeated with ambient air as well as pure liquid water. By comparing the number of counts measured with the each respective medium, the void fraction of the two-phase flow is measured as (Vince and Fincke, 1983):

$$\alpha_g = \frac{\ln(I_{2\phi} / I_l)}{\ln(I_g / I_l)} \quad (2.60)$$

where the counts are denoted by I where the subscript denotes the respective phase of the flow. However, there is uncertainty in this calculation due to the statistical fluctuations of radioactivity. The statistical variations are Poisson distributed and the uncertainty, ΔI, is approximately,

$$\Delta I \cong I N^{-1/2} \quad (2.61)$$

where N is the product of the number of counts measured and the number of repeated count measurements. Therefore, the longer the measurement time interval and the more times it is repeated, the smaller the error; and the gamma-ray measurements will become sensitive to even small void fractions. The margin of error is determined as (Vince and Fincke, 1983):

$$\frac{\Delta\alpha}{\alpha} = \frac{1}{\sqrt{I_{2\phi} n}} \frac{\left[2\left(1-\alpha+\alpha^2\right)\right]^{1/2}}{\alpha \ln\left(I_g / I_l\right)} \quad (2.62)$$

where n is the number of times the experiment has been repeated (Lindsay et al., 1995). Once the void fraction is obtained with the desired margin of error, as the name suggests, the two-phase density is calculated using this simple equation

$$\rho_{2\phi} = \alpha\rho_g + (1-\alpha)\rho_l \,. \quad (2.63)$$

The gamma-ray densitometer is a desirable means to measure the void fraction of two-phase flow for a number of reasons. The first reason is that the gamma-ray densitometer technique is non-intrusive. Measuring the void fraction of a two-phase flow should be done by non-intrusive means; otherwise, there would be interactions between the flow and the probe, which could lead to errors. The three most commonly used types

of radiation in the radiation attenuation method are neutrons, x-rays, and gamma-rays. Neutron based attenuation is costly due to the expensive source material such as man-made Cf-252. In addition, the safety precautions needed to adequately shield the surrounding environment from neutron radiation are both cumbersome and costly. X-ray based attenuation also requires a good deal of shielding due to the method in which x-rays are generated. More importantly, the x-rays have intensity fluctuations. As previously discussed, the radiation beam is desired to be mono-energetic (Stahl and von Rohr, 2004); therefore, the fluctuations are undesirable.

The source material used in our densitometer is Americium-241 (Am-241). Am-241 is a widely used radioisotope made from the β decay of Plutonium-241. Am-241 emits high energy α particles as well as mono-energetic, low energy γ rays. The alpha particles are easily shielded and do not pose an external hazard.

CHAPTER III

EXPERIMENTAL SETUP AND PROCEDURES

III.1. EXPERIMENTAL COMPONENTS

Below is a table listing the components used in the experiments.

Table 3.1: Hardware components

Label	Description	Manufacturer	Model
A	1000-liter water reservoir		
B	Centrifugal pump with 1.0 HP motor	Beldor	CL3509
C	Water flow meter with 0-80 gpm range	King Instruments	7205-0241-W
D	Control Valve – 175 psi	Milwaukee Valve	Co BB2
E	Pressure Gauge – 0-15 psig	Weiss	
F	Rotameter - 0-4.8 L/min at STP	Brooks	1355-01C1AAA
G	Pressure Gauge – 0-60 psig	Ashcroft	
H	Rotameter - 0-44L/min at STP	Brooks	1355-01C1AAA
	Vertical Movement Adjuster	NRC	370

III.1.1. Hardware Overview

III.1.1.1. Gamma-Ray Densitometer

The gamma-ray densitometer consists of a 45 mCi Americium 241 source encased in lead shielding. A switch is mounted onto the case with a small hole. When the switch is opened, the source is exposed through the small hole. A lock pin is placed on the switch to prevent accidental opening of the switch.

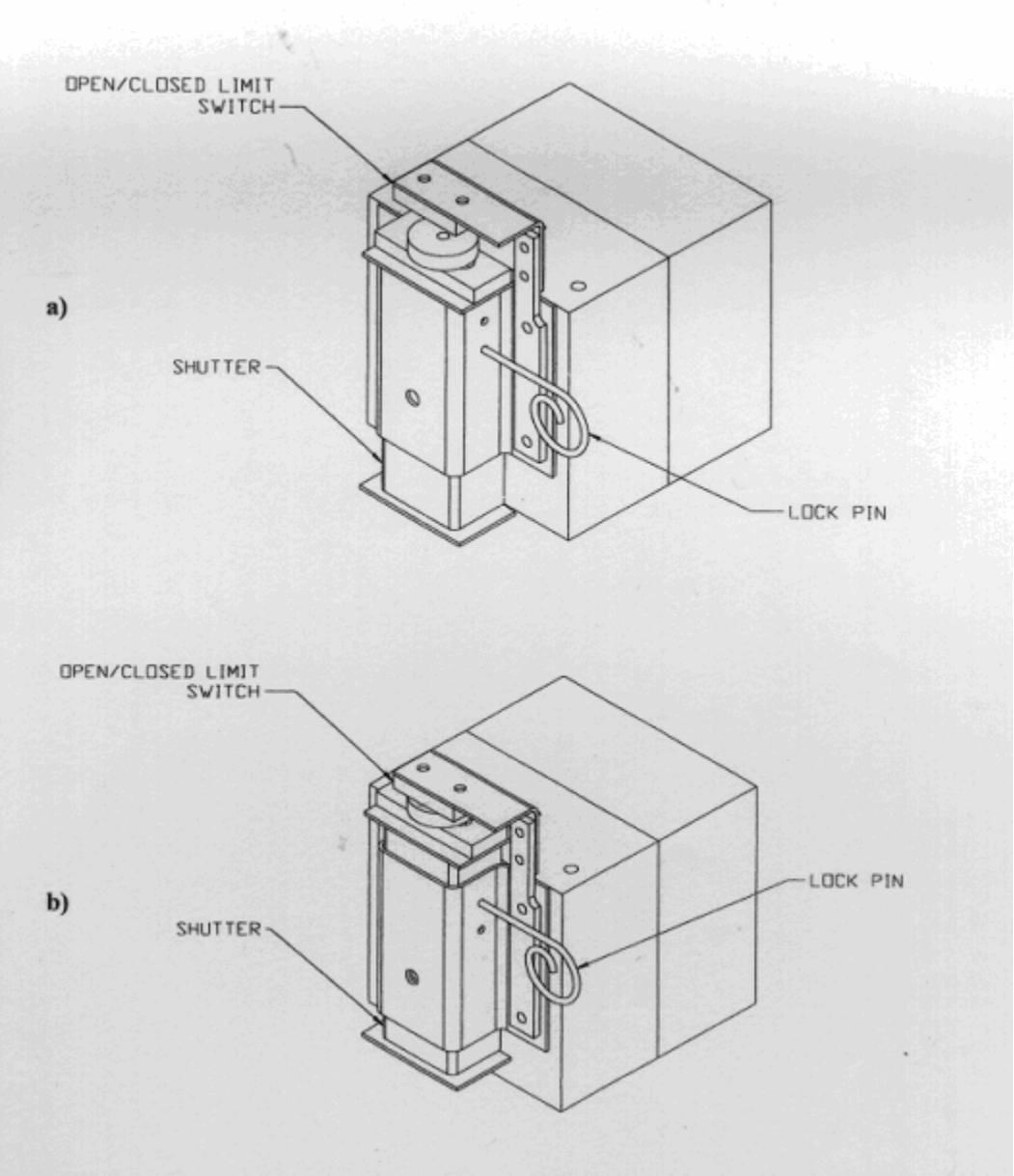

Figure 3.1: a: Source with shutter closed; b: source with shutter open

Mounting brackets are attached to the gamma-ray densitometer. The mounting brackets serve two purposes: firstly to mount the densitometer in position and secondly, to provide a brace to hold the radiation detector in place.

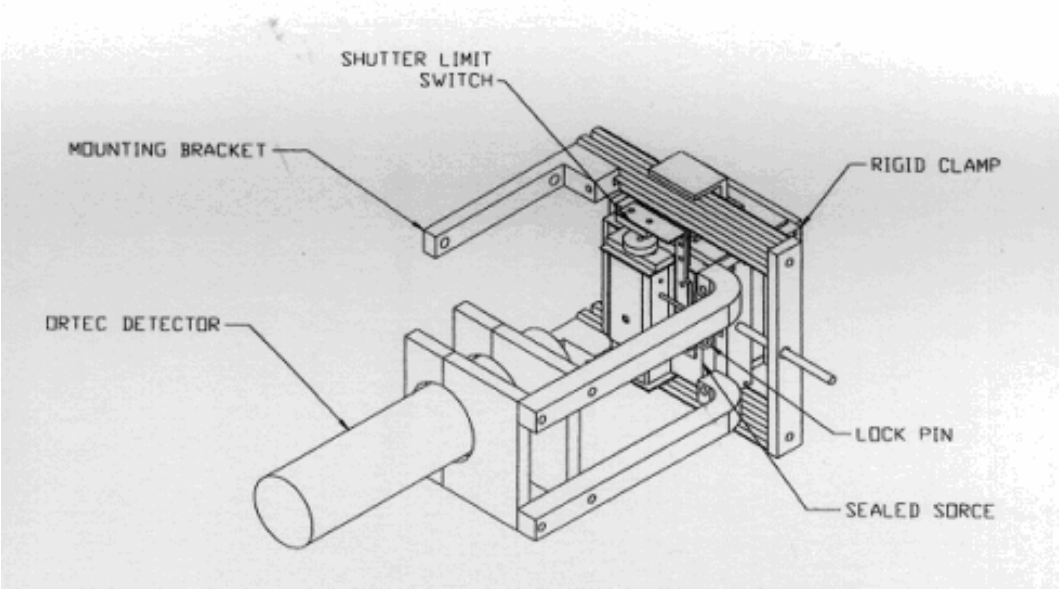

Figure 3.2: Gamma-ray densitometer with mounting equipment

The mounting bracket of the densitometer is then fastened onto a mounting plate. The mounting plate is fastened onto a vertical movement adjuster (NRC Model 370).

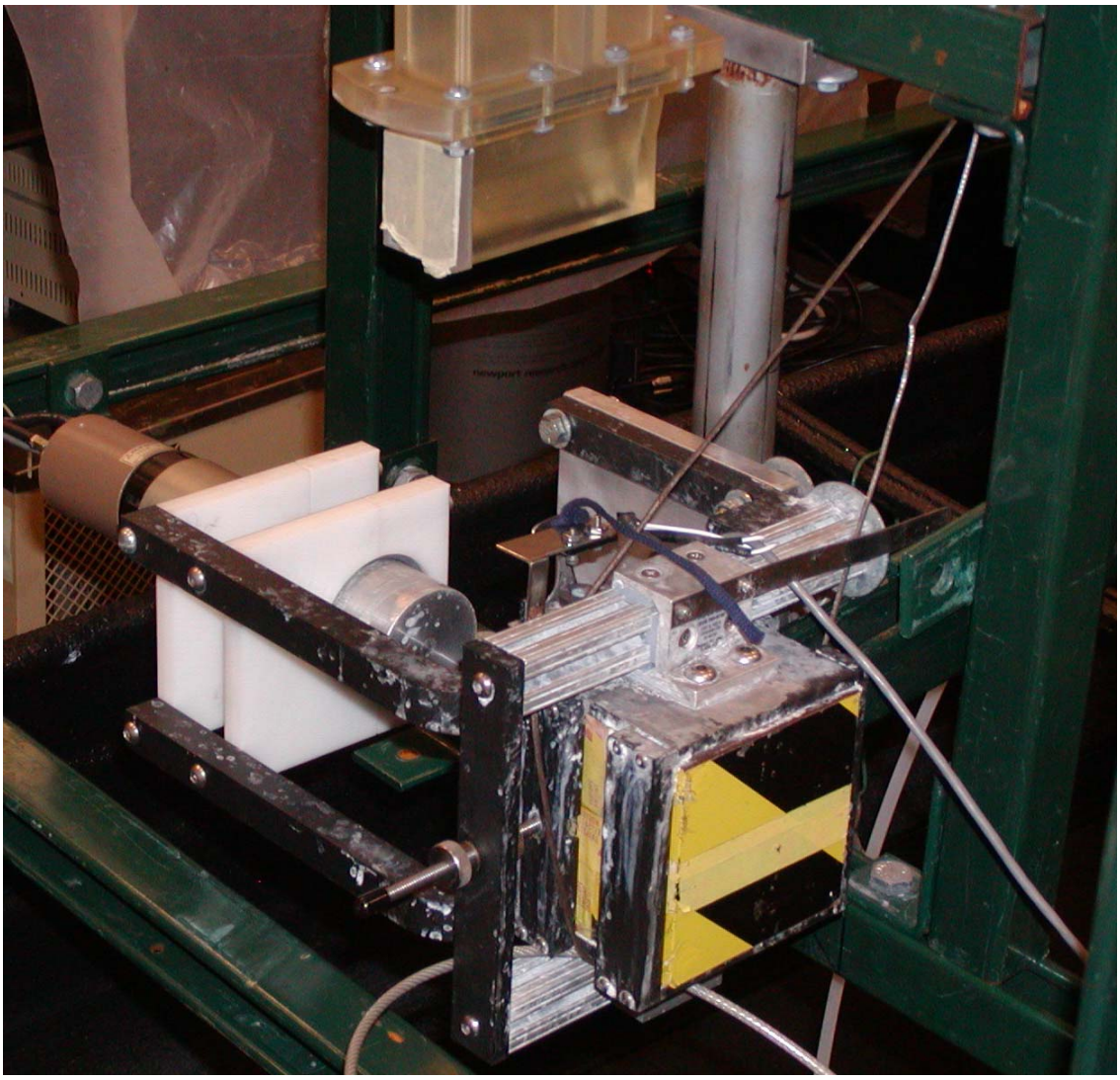

Figure 3.3: Gamma-ray densitometer fully mounted

III.1.1.2. Containers

A container was needed to hold water for the calibration of the densitometer. A rectangular container (with an open top) of inner dimensions 6.35 cm x 12.7 cm x 25.4 cm (2.5” x 5” x 10”) was constructed from 0.635 cm (¼”) thick PVC. Another container of identical dimensions and material was built, but this container lacked a top and bottom.

This container was used for the air calibration of the densitometer as well as for running plunging jet experiments.

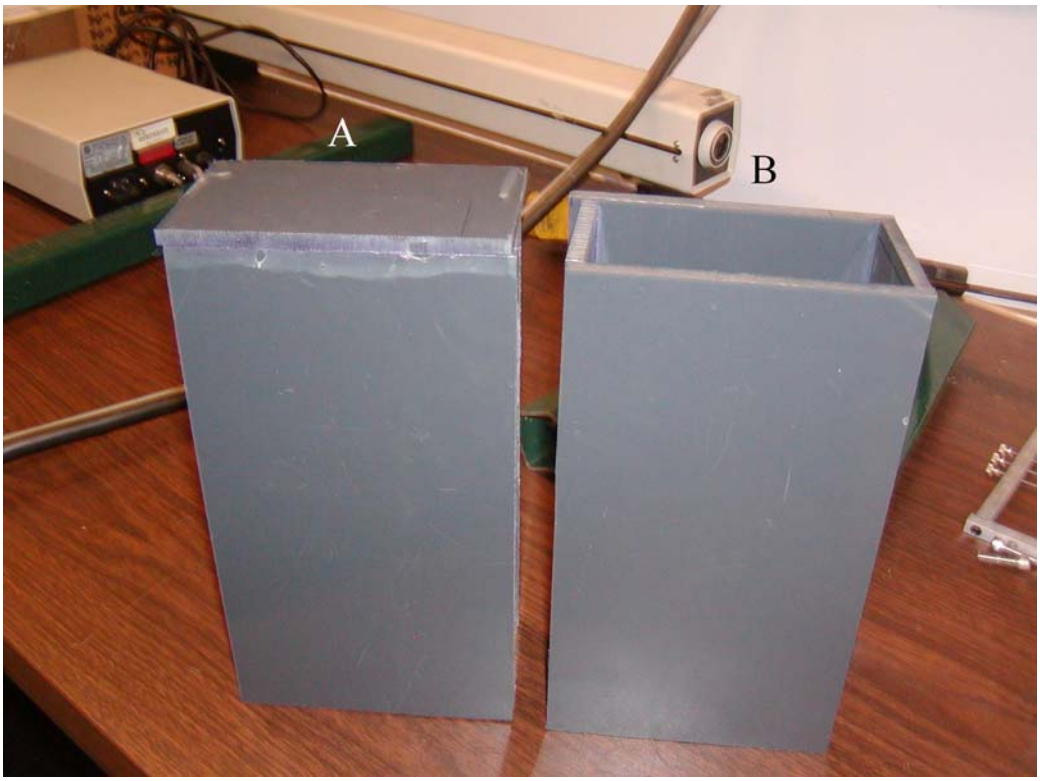

Figure 3.4: Containers (A – with bottom; B – without bottom)

III.1.1.3. Nozzle

The nozzle used produces a planar jet with initial dimensions (i.e., dimensions at exit from its source nozzle) of 10 cm x 1 cm. The nozzle was constructed from Vantico SL 7510, which is a resin with similar mechanical properties to ABS plastics. The surface roughness of the nozzle material is very small as the average peak-to-valley height is 5 microns, which should make any free-surface fluctuations negligible.

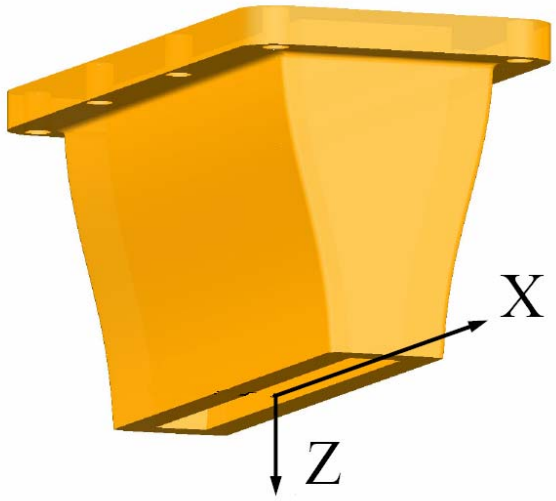

Figure 3.5: Coordinate system at nozzle exit

III.1.1.4. Flow Conditioner

The nozzle is fastened to a flow conditioner (see Figure 3.6). The flow conditioner is important as it reduces cross-stream flow and the effects of turbulence by breaking up eddies. It consists of several perforated plates and honeycomb sections followed by fine mesh screens downstream.

Table 3.2: Flow conditioner sections

Designation	Description	Resin	z-dimension (cm)
1	PP – HC section: Round to rectangle adapter	DSM Somos 7100	6.9
2A	Primary Screen flange	DSM Somos 7100	0.9
3	Calming chamber	Vantico 7510	13.8

Table 3.3: Flow conditioning elements

Designation	Element Type	Description
PP	Perforated Plate	50% open area with 4.8 mm staggered holes
HC	Honeycomb	3.2 mm diameter x 25.4 mm circular cells
FS-A	Fine Screen (30 x 30)	37.1% open area, 0.33 mm wire diameter with cell width 0.51 mm

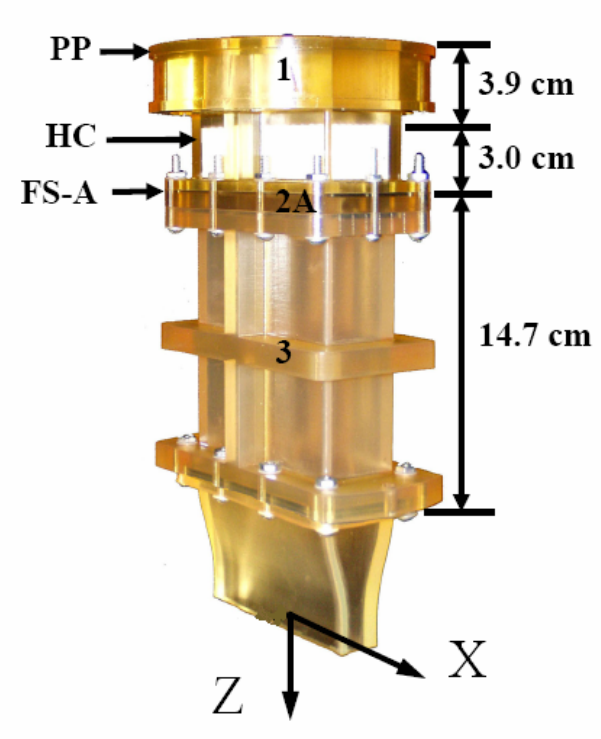

Figure 3.6: Flow conditioner with nozzle attached

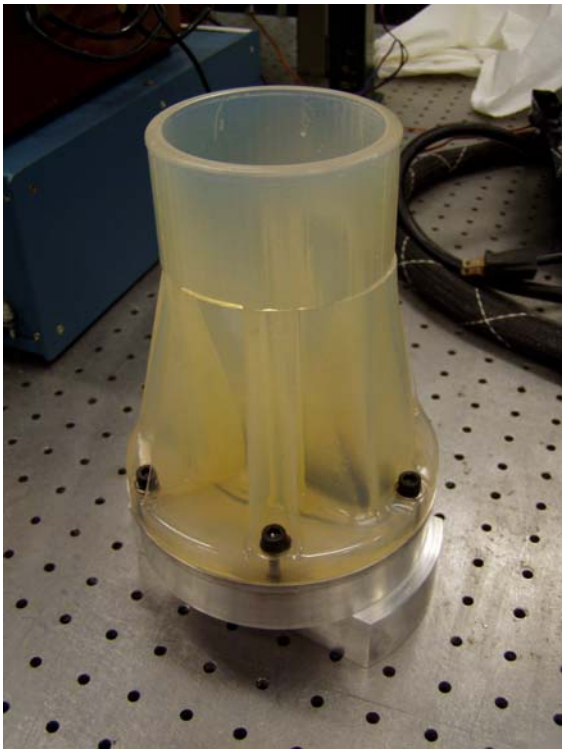

Figure 3.7: Flow conditioner mounting unit

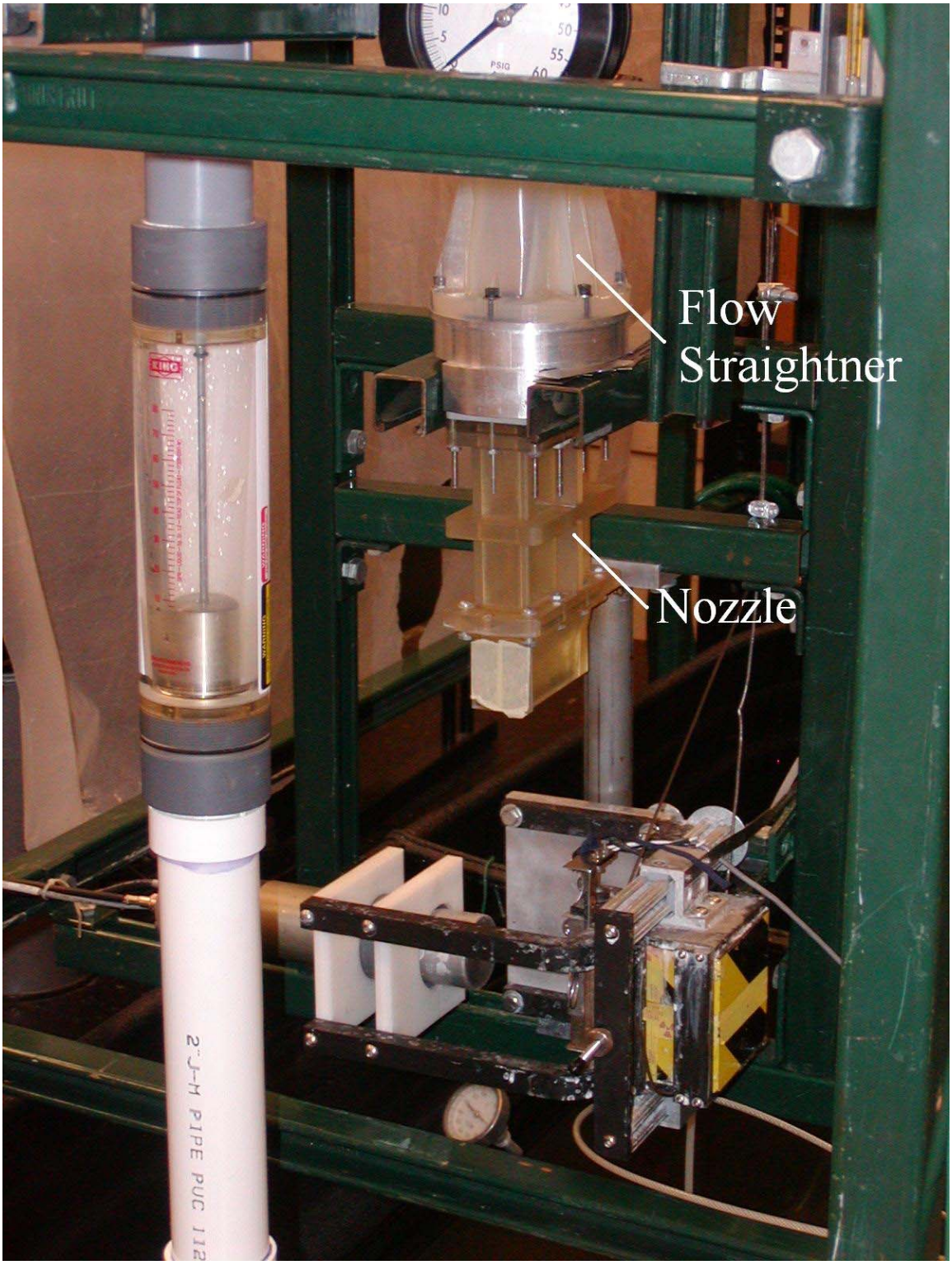

Figure 3.8: Mounted flow conditioner and nozzle

III.1.1.5. Jet Thickness Tester

The jet thickness tester is a rectangular frame made from 0.953 cm (3/8”) square aluminum bar stock. One of the smaller sides is mounted to the vertical movement adjuster via the same mounting plate that was used to mount the gamma-ray densitometer. It has three screw holes on each of the larger sides corresponding to where the densitometer measurements took place (the centerline and an offset distance on both sides of the centerline). Screws with a very fine thread were used in order to determine the jet thickness.

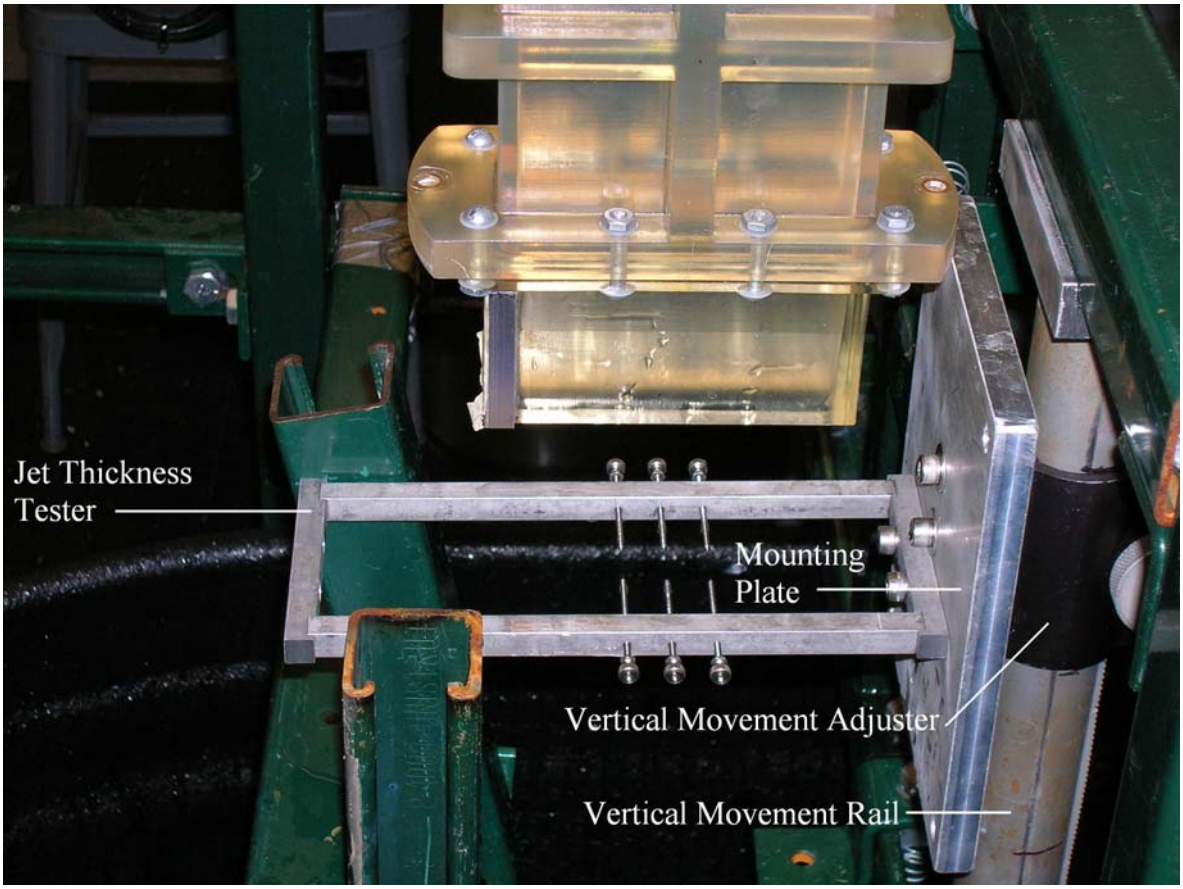

Figure 3.9: Mounted jet thickness tester

III.1.2. Instrumentation Overview

III.1.2.1. Radiation Instruments

Numerous radiation instruments are needed to measure the number of radiation events originating from the source, which are absorbed by the detector. The first instrument is an Ortec model 276 photomultiplier detector. Electrical power is supplied to the detector using an EG&G Ortec model 278 2-kV bias voltage supply. However, an amplifier is also used – EG&G Ortec model 590A amplifier and timing single-channel analyzer (SCA). Lastly the radiation data from the detector is processed through an Ortec model 871 timer and counter.

Figure 3.10: Radiation detection station

III.1.2.2. Flow Meters

Two Brooks rotameters were mounted in series with a pressure gauge mounted in between them to measure the pressure drop of air. The first rotameter is capable of measuring 0-44 L/min at STP and the second 0-4.8 L/min at STP for fine tuning.

III.1.2.3. Micrometer

A Lufkin depth micrometer was used in order to measure the distance from the screw-head to the side of the jet thickness tester.

II.2. FLOW LOOP CONFIGURATIONS

A 1000 liter tank is used as a reservoir for the experiment. The water from the reservoir is pulled out using a centrifugal pump (Beldor, Model # CL3509 with a 1.0 HP Motor) through a 5.08 cm (2”) diameter suction line. The pump discharge line includes a water flow meter (King Instruments, Model #7205-0271-W capable of 0-80 gpm range); a shutoff valve; a mixing, “Y” shaped area where gas is introduced to the flow; a flow conditioner; and a nozzle. The flow conditioner consists of several parts: a perforated plate, a honeycomb section, and a fine-mesh screen. In addition, a boundary-layer cutter is place at the nozzle’s exit.

Air is provided to the flow via an air compressor connected to a regulated line. The flow meters used are connected in series (Brooks Model #1355-01C1AAA, 0-43.8 and 0-4.84 L/min at STP). The gas is then connected to the “Y” shaped area mentioned above where it travels through a stainless steel porous tube into the water flow. The dimensions of the porous tube are an outer diameter of 0.794 cm (5/16”) and an inner diameter of 0.476 cm (3/16”). The gas flows through the 13 cm long non-porous entry part of the tube followed by a 20 cm long porous section. The end of that section is plugged to ensure uniform gas dispersion into the water.

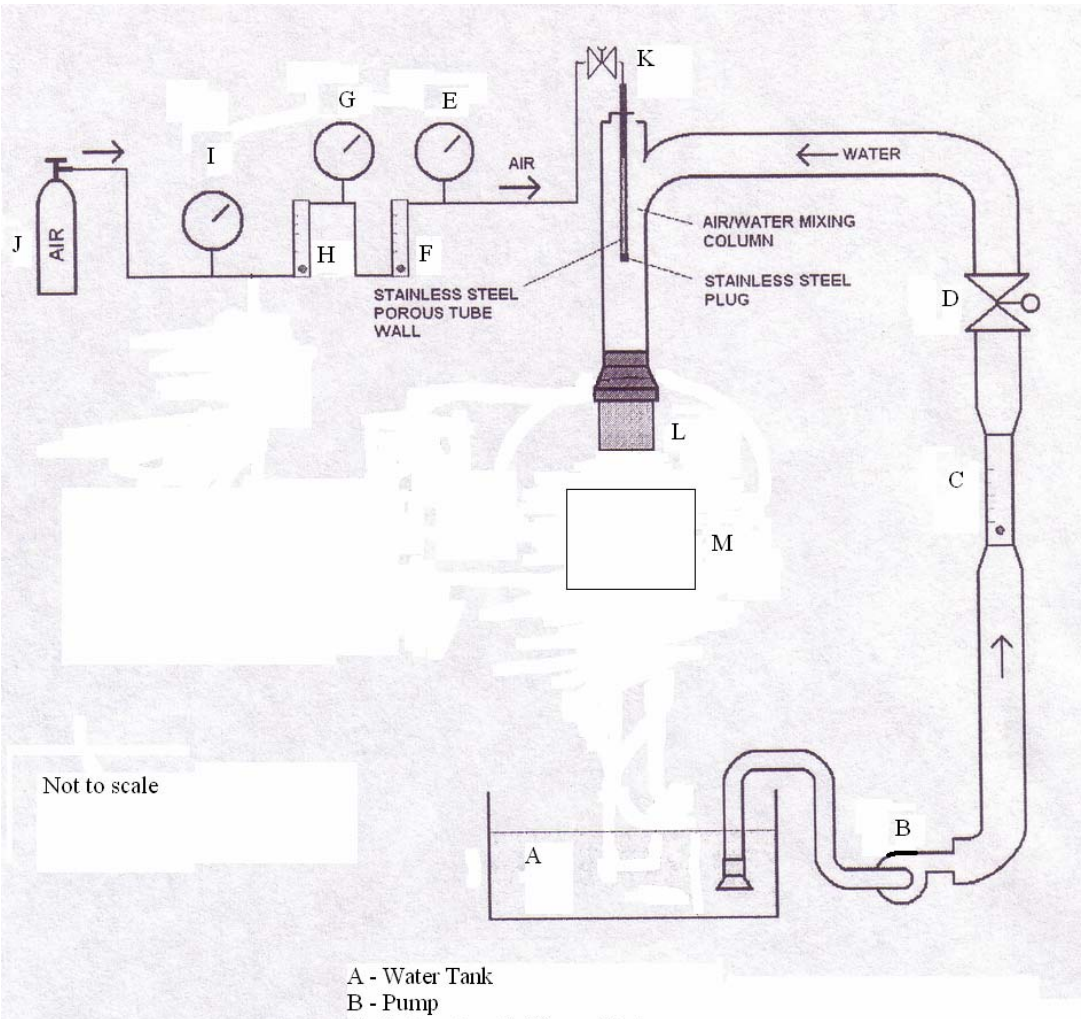

A - Water Tank
B - Pump
C - Rotameter - 0-80 gpm Water
D - Water Control Valve
E - Pressure Gauge - 0-15 psig
F - Rotameter - 0-4.8 L/min Air
G - Pressure Gauge - 0-60 psig
H - Rotameter - 0-44 L/min Air
I - Presssure Gauge 0-60 psig
J - Air Tank/Regulator
K - Ball Valve
L - Nozzle
M - Measurement Device
Gamma-Ray Densitometer OR
Jet Thickness Tester

Figure 3.11: Flow loop

III.3. EXPERIMENTAL PROCEDURES

III.3.1 Calibration

Calibration of the gamma-ray densitometer is crucial in order to ensure the accuracy of the experiment. Properties such as the room temperature and relative humidity can change over time. Calibrations are performed before and after the experimental trials, and are repeated for each day of the experimental trial. A container is placed between the detector and source and filled with room temperature water. The gamma-ray densitometer is used for five minutes and the number of counts, denoted I_l is recorded. The water-filled container is then replaced with the bottomless container containing ambient air and again the gamma-ray densitometer is used for five minutes and the number of counts, denoted I_g is recorded. The calibration values of I_l and I_g are averaged for each experimental trial (one set of I_l and I_g were taken before the experiment and another set of I_l and I_g were taken after the experiment) and the values of these averages are used in order to calculate the void fraction of the flow for measurements taken that day.

In order to determine if a five minute counting interval is appropriate for the calibration, ten, five minute counts were taken for both the water-filled container and the empty container. The results from this study are that the standard deviation divided by the average is 0.522% for I_l 0.171% for I_g. Therefore, it was concluded that a five minute counting time for the calibration of the gamma-ray densitometer is sufficient.

III.3.2. Error Sources

Limiting the potential error sources is essential not only for the accuracy of these experiments, but also the repeatability. The first error source is the calibration of the gamma-ray densitometer source, air and water count measurements will change over time. Calibrations must be done daily when the experiments are run. Before the gamma-ray densitometer is used; the counter is visually inspected to make sure all the dials are in the proper settings. If the detector is receiving too much or too little voltage from the voltage source and amplifier, it will affect the number of counts, and thus compromise the experiment. Moreover, the counting window must remain the same between experiments.

III.3.3. Tank Filling

The reservoir must be emptied weekly as particles and algae may compromise the experiment. Once the pool is filled with cold water, the water must be allowed to reach room temperature in order to ensure repeatability.

III.3.4. Experimental Trials – Void Fraction

Once the air and water calibrations are complete, one can begin the experimental trials. The first step is to place the bottomless container between the source and detector. Next, the source is moved into place on the x-axis via the sliding rail bar located on the

densitometer. The rail allows for a travel of 2.86 cm. There are a total of three x locations that trial runs were taken – the centerline of the jet (denoted the coordinate “0”), and positions offset from the centerline of 1.43 cm on both sides (denoted the coordinates “-1.43” and “1.43”) (see Figure 3.5 for the definition of the coordinates). The densitometer unit is then moved in place vertically via the vertical movement rail it is mounted to. The rail allows for a travel of 16.5 cm. There are a total of three z locations that trial runs were taken – the highest point was 5.4 cm from the nozzle’s exit (this was as close as one could get given the size of the densitometer), 13.7 cm from the nozzle’s exit, and 21.9 cm from the nozzle’s exit.

After the densitometer is moved in place, the pump is turned on, and the volumetric flow rate of water is regulated. There are a total of five water flow rates used for the experiment. The maximum flow rate of water used in the equipment was 288 L/min (76 gpm), which is equivalent to a velocity of 4.79 m/s at the nozzle exit. The other measured water flow rates were 240 L/min (63.5 gpm) (4 m/s nozzle exit velocity), 180 L/min (47.6 gpm) (3 m/s nozzle exit velocity), 120 L/min (31.7 gpm) (2 m/s nozzle exit velocity), and 60 L/min (15.9 gpm) (1 m/s nozzle exit velocity). Once the desired flow rate of water is set, air is injected into water.

Once air is injected into the nozzle, a two-phase flow field generates upstream the nozzle exit. The flow regime in the nozzle is important. If the flow regime in the nozzle is anything other than bubble flow, the jet will be unstable. The requirement of bubbly flow regime upstream the nozzle leads to some restriction with respect to feasible ranges of the gas and liquid flow rates in the tests.

The injected air was determined by the ratio of the volumetric flow rate of air to that of water. For 1 m/s flow, no air was added since the resulting flow regime would be an undesired slug flow in the nozzle. For 2 m/s flow, air was added at a ratio of flow rates of Q_g / Q_l = 1.25%, and this value was visually determined to be the maximum value before the transition to slug flow took place. For 3 m/s, 4 m/s, and 4.79 m/s flow, air was added at a ratio of flow rates (Q_g / Q_l) equal to 2.5%, 5%, 10%, 15%; air was also added at a ratio of 20% for the 4 m/s and 4.79 m/s flow. Therefore there were a total of 20 experiments (5 liquid-only and 15 two-phase) and these experiments were run at a total of nine positions, resulting in 180 data points.

Once the desired flow is obtained, one minute is allowed to elapse for the flow to reach steady state, which is confirmed visually as well. The densitometer is then used for five minutes and the number of counts, denoted as I is recorded. The experiments are repeated until a total of 20 flows are taken at all nine positions.

III.3.5. Experimental Trials – Jet Thickness

Once the counts have been recorded for all positions and flow rates, the gamma-ray densitometer is removed from the vertical movement rail. The jet thickness apparatus is then fastened onto the vertical movement rail, which will allow it to undergo vertical movement. The apparatus was designed such that the three screws on each side correspond to the three locations in relation to the jet where the densitometer measurements were taken. Using to aforementioned method, the jet is turned on and the desired water and air flows are set. The screws are turned towards the jet until a wake is

formed from touching the jet. The screws are then turned away, until the wake is at its faintest. Using a depth micrometer, the distance from the screw head to the side of the apparatus is measured for all three screws on both sides (denoted 1_a, 1_b, 2_a, 2_b, 3_a, and 3_b in Figure 3.2)

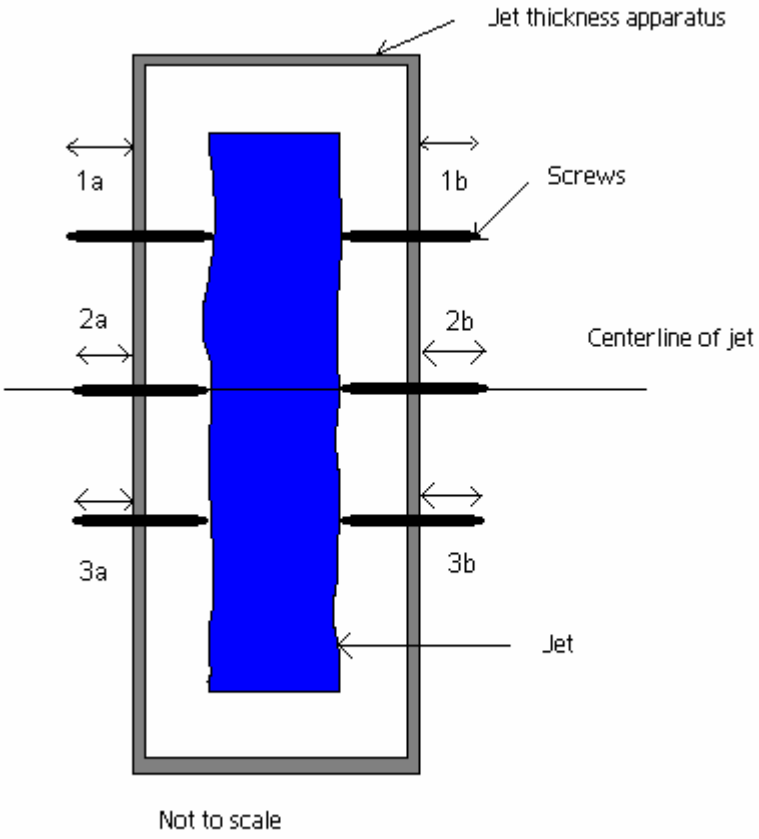

Figure 3.12: Jet thickness measurements

The trials are repeated until all 20 experiments are run at all three vertical locations. The next step is to turn the screws in until they touch each other (with of course, the jet turned off). Again, the distance from the screw head to the side of the

apparatus is measured for all three screws on both sides. These "calibration" measurements are recorded C_{1a}, C_{1b}, C_{2a}, C_{2b}, C_{3a}, and C_{3b}. The thickness of the jet at position 1 is then simply

$$t_{POS\_1} = \left(1_a - C_{1a}\right) + \left(1_b - C_{1b}\right) \quad (3.1)$$

III.3.6. Experimental Trials – Jet Width

The width of the jet was measured by first taking a picture with a digital camera with zoom capabilities (Olympus C700). Once the picture file was transferred onto a computer, the picture was scaled by measuring the number of pixels wide the nozzle spans (using an on-screen ruler) and comparing to the known nozzle width. At the three different fixed distances from the nozzle exit, the jet width was measured via the on-screen ruler (JRuler). An example of a picture taken for measuring the jet width is shown in Figure 3.13.

Figure 3.13: A typical jet width picture

CHAPTER IV

RESULTS AND DISCUSSIONS

IV.1. TEST MATRIX

Table 4.1: Experiments conducted

Experiment	Water Flow (Q_l) in L/min and (gpm) and Inlet Liquid Velocity (U_l) in m/s	Gas Flow (Q_g) in L/min	Q_g / Q_l (%)
1	60; (15.9); 1	0	0
2	120; (31.7); 2	0	0
3	180; (47.6); 3	0	0
4	240; (63.5); 4	0	0
5	288; (76); 4.79	0	0
6	120; (31.7); 2	1.5	1.25
7	180; (47.6); 3	4.5	2.5
8	240; (63.5); 4	6	2.5
9	288; (76); 4.79	7.2	2.5
10	180; (47.6); 3	9	5
11	240; (63.5); 4	12	5
12	288; (76); 4.79	14.4	5
13	180; (47.6); 3	18	10
14	240; (63.5); 4	24	10
15	288; (76); 4.79	28.8	10
16	180; (47.6); 3	27	15
17	240; (63.5); 4	36	15
18	288; (76); 4.79	43.2	15
19	240; (63.5); 4	48	20
20	288; (76); 4.79	57.5	20

Table 4.1 is a summary of the experimental runs. Note that in each experiment the jet void fraction and thickness were measured at nine points, namely three z values (5.4

cm, 13.7 cm and 21.9 cm) from the nozzle exit, and for each z, three x locations (0 cm, -1.43 cm and 1.43 cm) from the jet centerline (see Figure 3.5).

The gamma-ray densitometer and radiation detection station were used in order to measure the number of radiation counts for a total of 20 experiments. Five of the experiments were single phase water with initial velocities ranging from 1 m/s to the maximum value of the system of 4.79 m/s. The 15 two-phase experiments were done with initial gas fractions ranging from 1.25% to 20%. Thus, a total of 180 data points were recorded.

IV.2. VOID FRACTION

Using the calibration values of I_l and I_g the average void fraction across the container was calculated as

$$\overline{\varepsilon}_{g_c} = \frac{\ln\left(I_{2\phi} / I_l\right)}{\ln\left(I_g / I_l\right)} \quad . (4.1)$$

If the void fraction of the jet is assumed to be zero (in the case of single phase flow), the thickness of the jet can be determined from this technique. Moreover, regardless of the initial gas flow, the collapsed liquid thickness (denoted with subscript CLT) of the jet is determined using the following equation

$$\delta_{CLT} = L\left(1-\overline{\varepsilon}_{g_c}\right) \quad (4.2)$$

where L is the inner distance of the container (the span across which the void fraction was determined [6.35 cm]). The δ_{CLT} is plotted as a function of x position for a fixed z position for given water and air flow rates. When δ_{CLT} is plotted against x position, the

plot is asymmetric about the centerline. It is proposed that the asymmetry of the δ_{CLT} is due to asymmetry within the nozzle and flow straightener as opposed to the jet hydrodynamic phenomena.

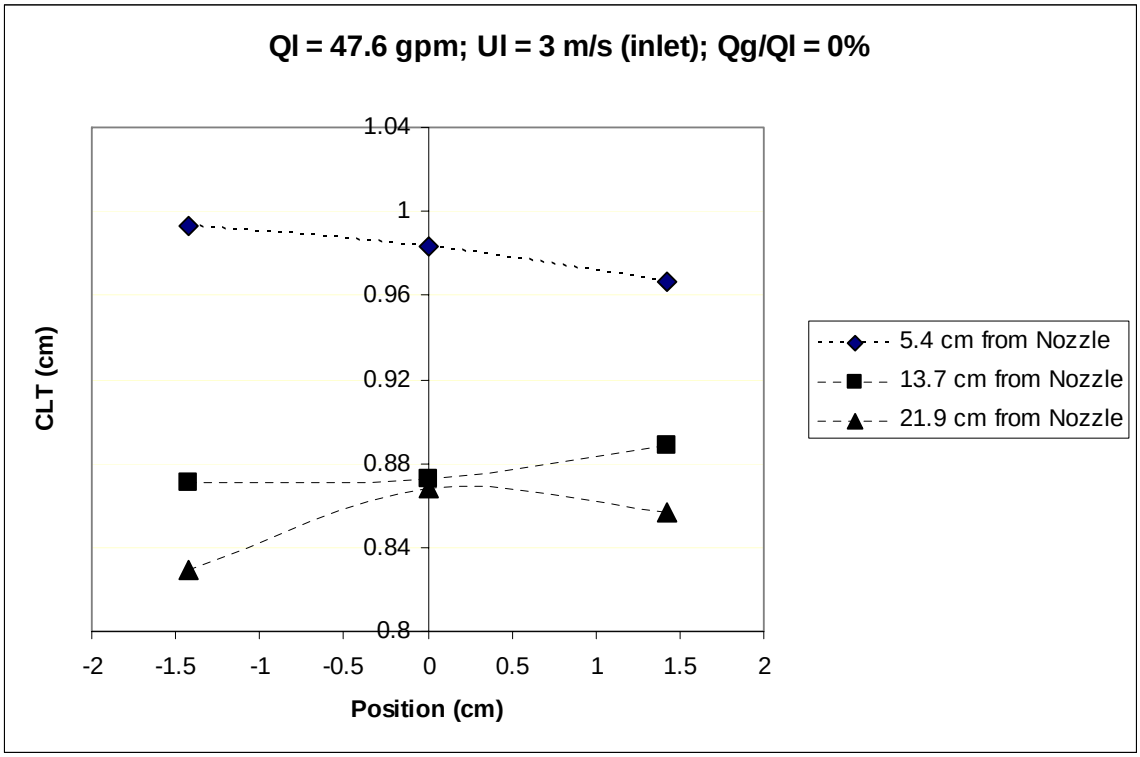

Figure 4.1: Collapsed liquid thickness versus x-position

Figure 4.1 shows a typical asymmetric profile. Asymmetry was observed independent of gas and liquid initial flow rates. The analysis of the void fraction and other such related parameters in this thesis will be one-dimensional (z-direction [distance from nozzle]) and x-averaged values will be used at each fixed z distance. Nevertheless, the occurrence of this asymmetry should be noted.

The experiments noted in Table 4.1 were repeated and the jet thickness was measured; and again the experiments were repeated and the photos needed for the jet width measurements were taken. The void fraction of the jet is then simply

$$\varepsilon_{g_j} = 1 - \left(\delta_{CLT} / \delta_{MT} \right) \quad (4.3)$$

where δ_{MT} is the measured thickness of the jet.

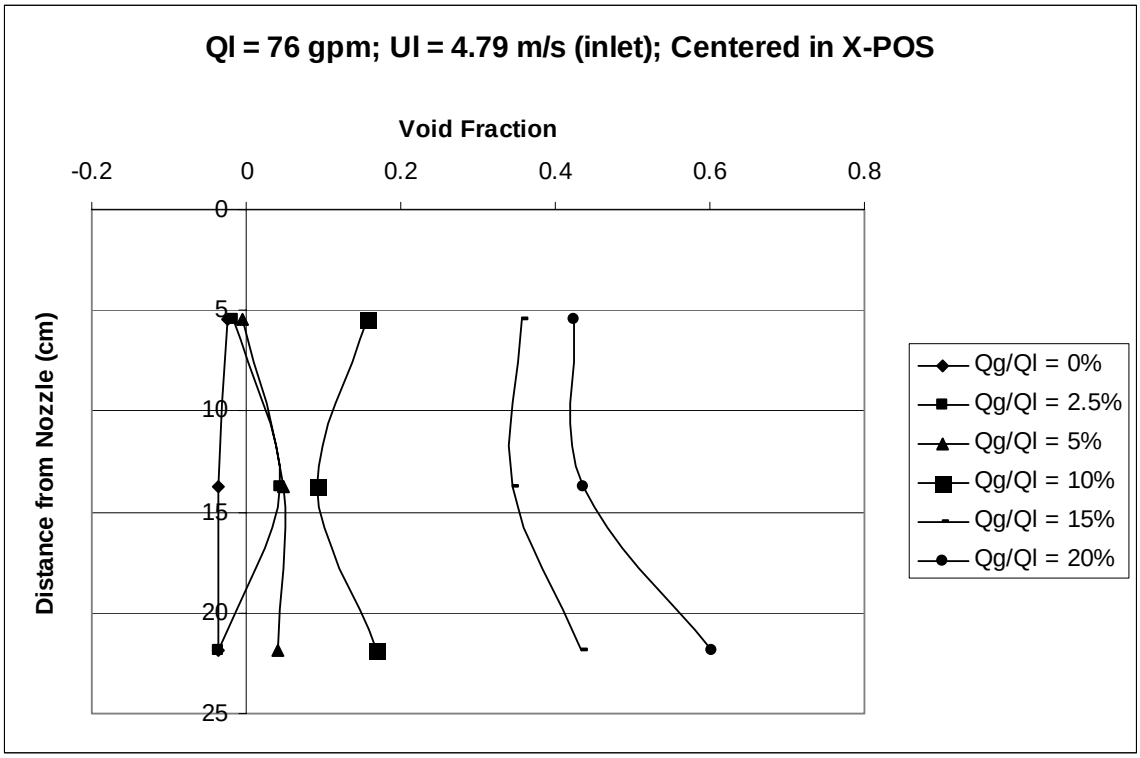

Figure 4.2: Void fraction versus distance from nozzle

In Figure 4.2, the void fraction of the jet is plotted against the distance from the nozzle for a fixed water flow rate. Each line corresponds to a specific gas flow rate. An atypical result of the void fraction calculations was that the void fraction was negative for low gas flow rates. The negative void fraction physically means that the collapsed liquid

thickness is greater than the measured jet thickness; therefore the collapsed liquid thickness has been overpredicted and or the measured thickness has been underpredicted. This suggests that the error associated with one or more facets of the measurements needed in the computation of the void is on the order of the void fraction or greater. The error associated with the measurement of the thickness of the jet, while small, is likely on the order of the void fraction measurements for the range of Q_g / Q_l = 0-5%. The other potential source of error is from liquid droplet deposition onto the walls on the container while the densitometer is in use. It is difficult to predict the amount of the droplet deposition, but it would lead to a slight overprediction of the collapsed liquid thickness.

The values of the void fraction for all experiments are given in the Appendix C, but due to the aforementioned error, only the high gas flow rate experiments (resulting in void fractions of 10% and greater) are studied extensively.

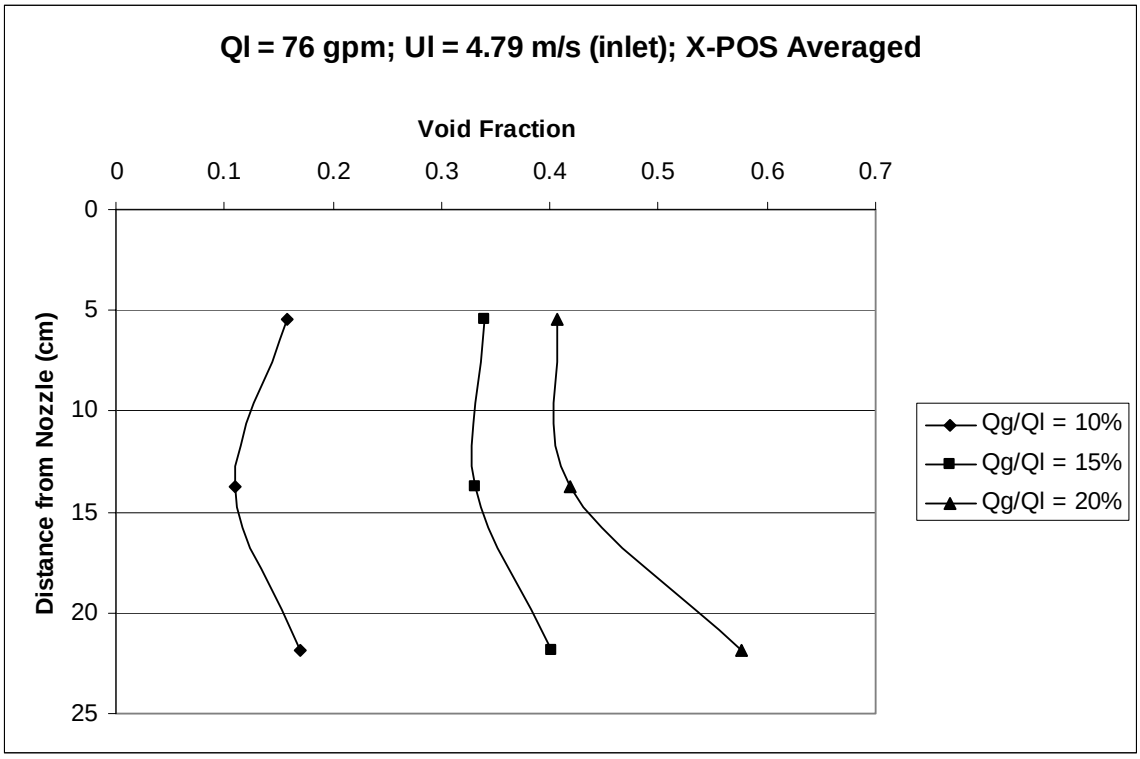

Figure 4.3: Void fraction versus distance from nozzle

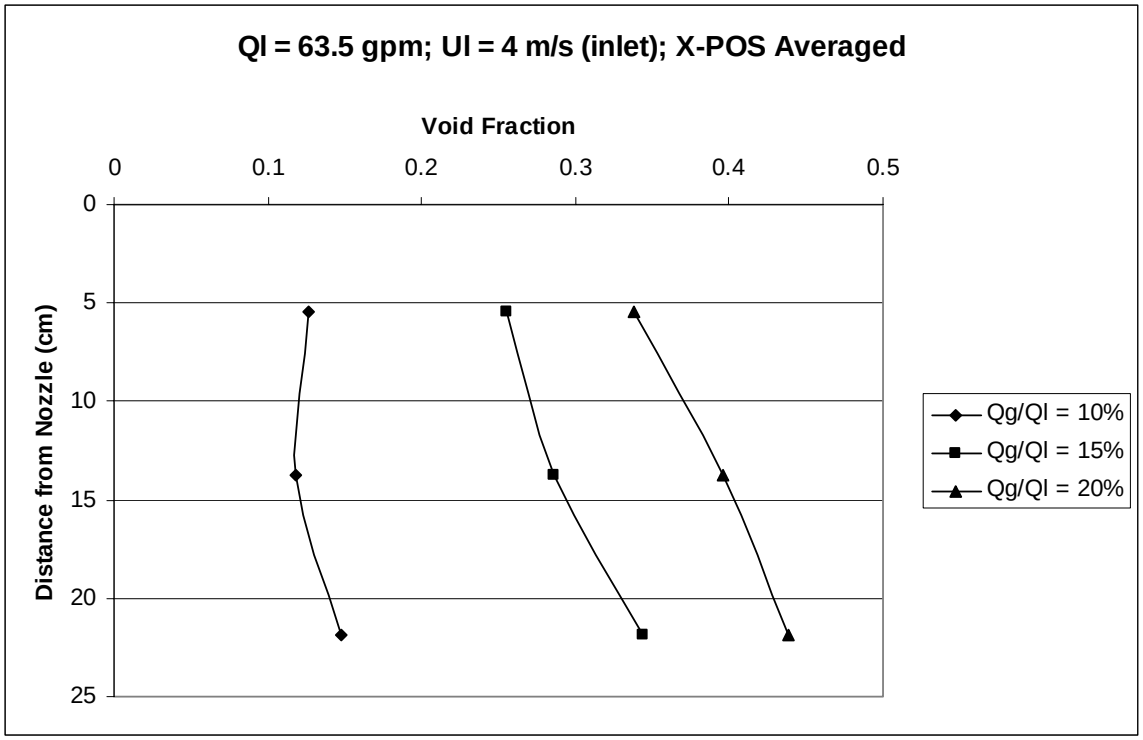

Figure 4.4: Void fraction versus distance from nozzle

Figures 4.3 and 4.4 display the six high gas flow rate experiments studied. The void fractions ranged from below 10% to almost 60%. The void fraction increases with increasing the initial gas flow rate – an expected trend. An additional trend is that the void fraction increases with increasing distance from the nozzle. Therefore the slip ratio is decreasing since the liquid is accelerating downward, while the gas resists downward flow due to the buoyancy effect – this trend was also expected.

IV.3. VELOCITY SLIP

Once the collapsed liquid thickness, jet thickness and jet width are known, many hydrodynamic properties can be studied. The gas and liquid velocities are of interest for the slip ratio calculations, where

$$S = \frac{U_g}{U_l}, \quad (4.4)$$

$$U_g(z) = \frac{\delta_{in} w_{in} j_{g,in}}{\delta_{MT} w_{MT} \varepsilon_{g_j}}, \quad (4.5)$$

$$U_l(z) = \frac{\delta_{in} w_{in} j_{l,in}}{\delta_{MT} w_{MT} \left(1 - \varepsilon_{g_j}\right)} \quad (4.6)$$

where the "MT" subscript denotes measured values and the "in" subscript denotes nozzle dimensions. As previously discussed,

$$j_{g,in} = \frac{Q_g}{A_{in}}, \quad (4.7)$$

$$j_{l,in} = \frac{Q_l}{A_{in}} \quad (4.8)$$

where the area is simply

$$A_{in} = \delta_{in} w_{in}. \quad (4.9)$$

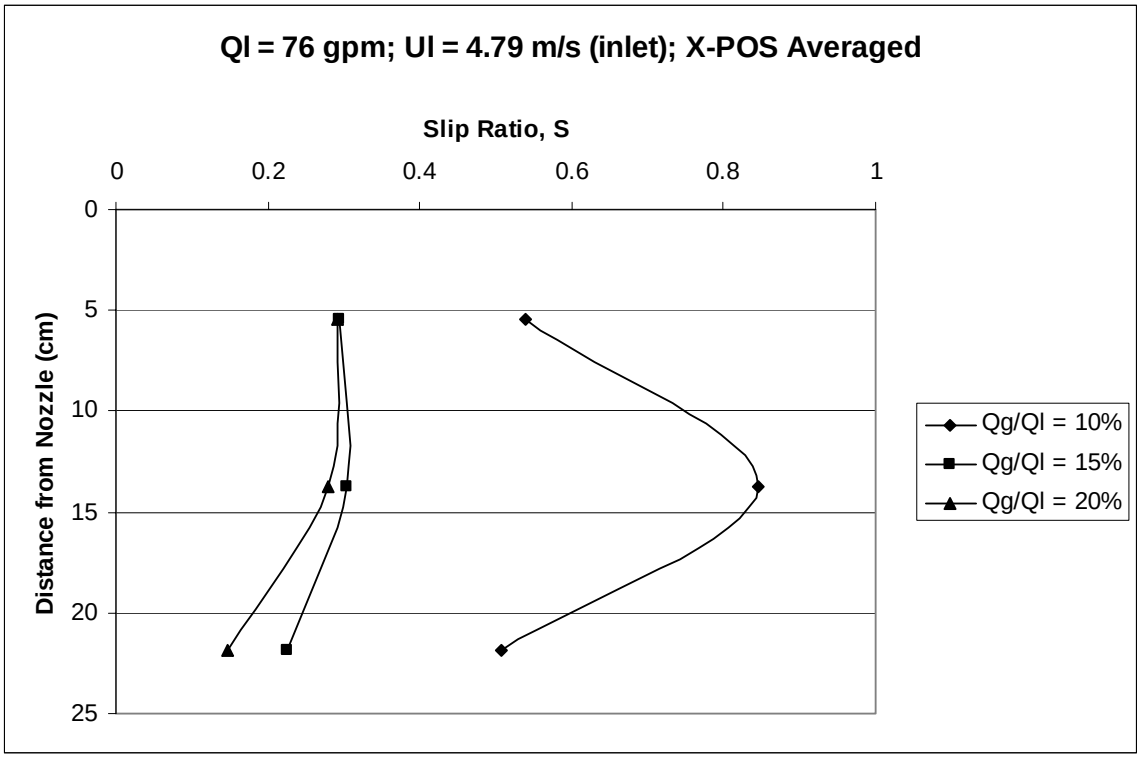

Figure 4.5: Slip ratio versus distance from nozzle

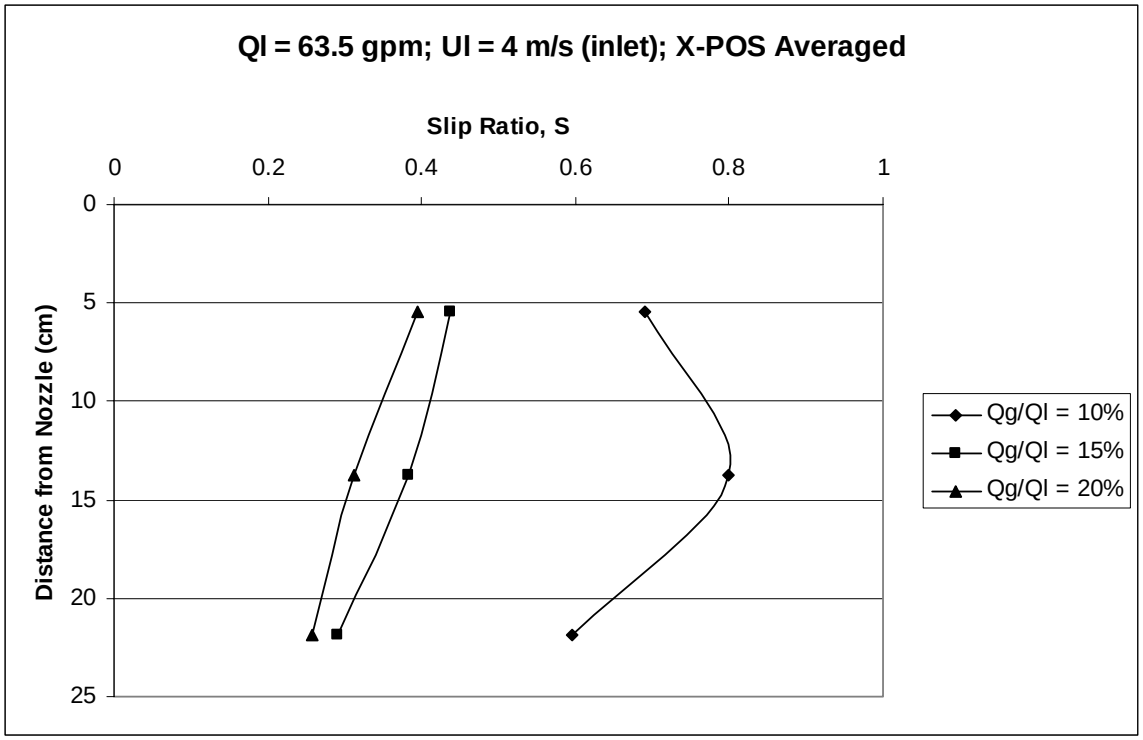

Figure 4.6: Slip ratio versus distance from nozzle

Figures 4.5 and 4.6 show the relationship between the slip ratio and the distance from the nozzle. The slip ratio values ranged from less than 0.2 to greater than 0.8. Thus, at no positions studied was the gas velocity greater than the liquid velocity. Generally as the distance from the nozzle increased, the slip ratio decreased, indicting the liquid is accelerating and or the gas is decelerating.

IV.4. EMPIRICAL CORRELATIONS IN PLUNGING JETS OR NOZZLES

As suggested by the literature, the void fraction in plunging jets or nozzles is dependent on several dimensionless parameters. These parameters are the liquid

Reynolds number, the Weber number, and the Froude number, and they are defined here as:

$$Re_l(z) = \frac{U_l \delta_{MT}}{\nu_l}, \quad (4.10)$$

$$We_l(z) = \frac{U_l^{\,2} \delta_{MT} \rho_l}{g_c \sigma} \quad (4.11)$$

and

$$Fr_l(z) = \frac{U_l^{\,2}}{g \delta_{MT}}. \quad (4.12)$$

The simplest form of an empirical correlation is

$$\frac{\varepsilon_g}{\varepsilon_{go}} = C_o Re^a Fr^b We^c D^{*d} \quad (4.13)$$

where C_o, a, b, c, and d are constants. D^* is a dimensionless distance defined as

$$D^* = \left(\frac{z}{\delta_{in}} \right) \quad (4.14)$$

where z is the distance from the nozzle and δ_{in} is the nozzle thickness (1 cm). ε_{go} is the homogeneous-flow void fraction at the nozzle exit defined as:

$$\frac{Q_{g_{in}}}{Q_{l_{in}} + Q_{g_{in}}}. \quad (4.15)$$

Using the numerical software, DataFit, the constants in the above correlation were optimized, leading to the following correlation:

$$\frac{\varepsilon_g}{\varepsilon_{go}} = 2.07 \times 10^{-1} \left[Re_l^{-9.91 \times 10^{-2}} Fr_l^{-0.591} We_l^{0.772} \right] \left(\frac{z}{\delta_{in}} \right)^{0.101}. \quad (4.16)$$

The strong dependence on the Weber number is largely attributed to the two free surfaces of the jet. The above correlation is in fact a relation among ε_g, Q_l, Q_g, δ_{MT} and w_{MT}, when the nozzle geometry and fluid properties are fixed. In terms of these parameters the correlation can be recant as:

$$\frac{\varepsilon_g}{\left(\frac{Q_{g_{in}}}{Q_{l_{in}}+Q_{g_{in}}}\right)} = 2.07\times10^{-1}\left[\left(\frac{\left(\frac{\delta_{in}w_{in}\left(\frac{Q_l}{\delta_{in}w_{in}}\right)}{\delta_{MT}w_{MT}\left(1-\varepsilon_g\right)}\right)\delta_{MT}}{\nu_l}\right)^{-9.91\times10^{-2}}\left(\frac{\left(\frac{\delta_{in}w_{in}\left(\frac{Q_l}{\delta_{in}w_{in}}\right)}{\delta_{MT}w_{MT}\left(1-\varepsilon_g\right)}\right)^2}{g\delta_{MT}}\right)^{-0.591}\left(\frac{\left(\frac{\delta_{in}w_{in}\left(\frac{Q_l}{\delta_{in}w_{in}}\right)}{\delta_{MT}w_{MT}\left(1-\varepsilon_g\right)}\right)^2\delta_{MT}\rho_l}{\sigma}\right)^{0.772}\right]\left(\frac{z}{\delta_{in}}\right)^{0.101} \quad (4.17)$$

The correlation has an R^2 fit of 0.95, and the correlation values of the void fraction are compared to the measured values of the void fraction.

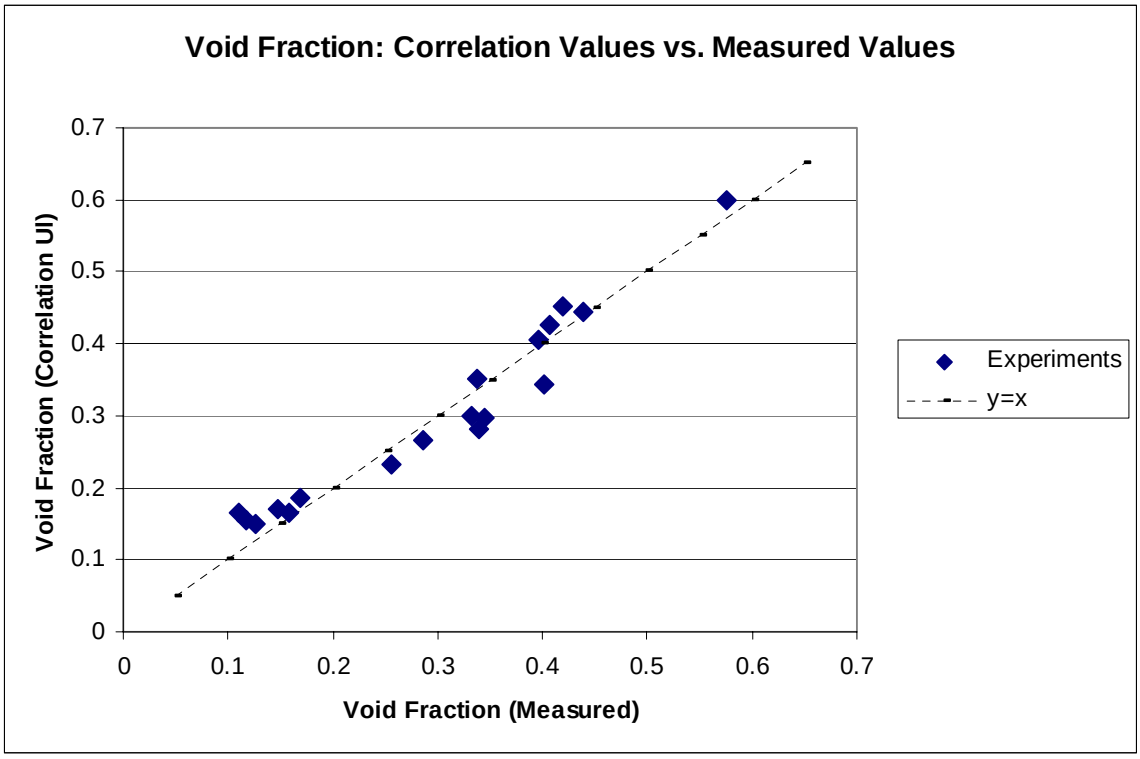

Figure 4.7: Measured void fraction versus correlation void fraction

The dashed line in figure 4.7 represents an exact agreement between the correlation and the measured values. It is of interest to identify which experiments were outliers.

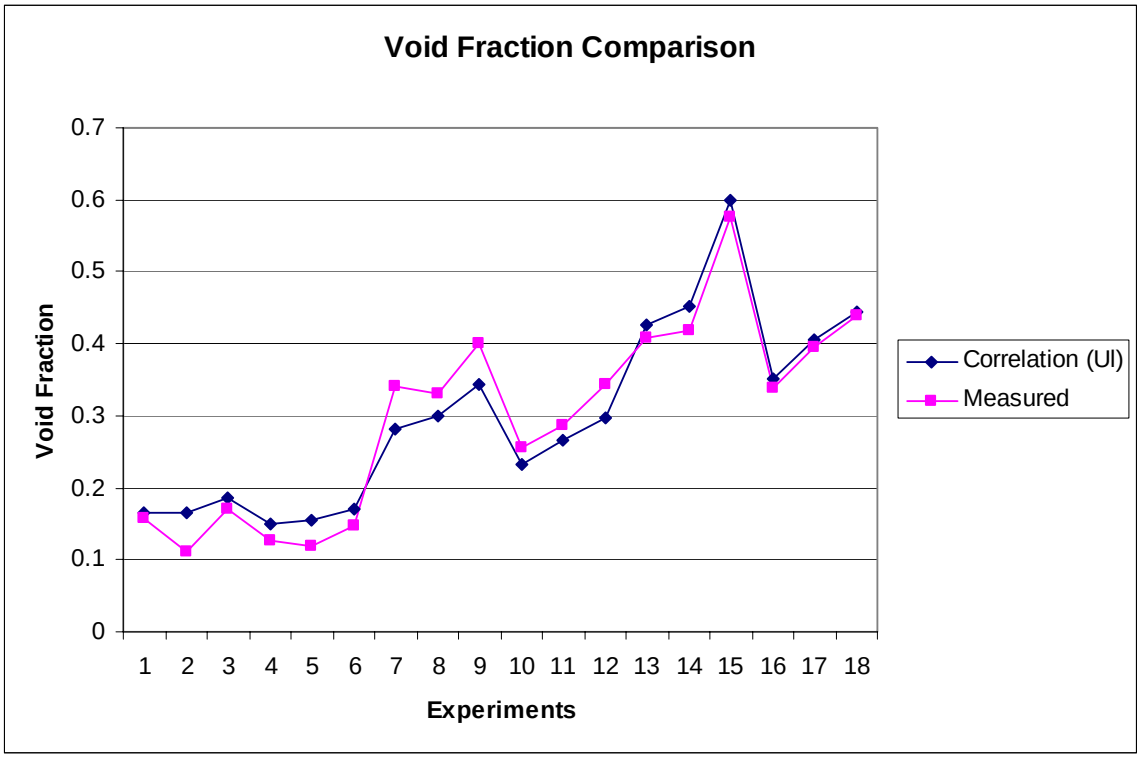

Figure 4.8: Void fraction comparison

Figure 4.8 is shown to compare the correlation and individual measured values of the void fraction. The x-axis is setup so that each experiment (unique initial water and air flow rates) are listed in groups of three, which correspond to the three different distances from the nozzle measured (increasing distances from the nozzle). Point 2 is an outlier since measured void fraction decreased compared to point 1 as the distance from the nozzle increased.

One disadvantageous feature of the aforementioned correlation is the need for iteration in order to solve for the void fraction. This is due to the dependence of the void fraction in the liquid velocity term used in the Reynolds, Weber, and Froude numbers. Rather than using the local velocity, the superficial velocity is modified such that

$$j_l = \frac{\delta_{in} w_{in} j_{l,in}}{\delta_{MT} w_{MT}} \text{ . (4.18)}$$

This term is used in lieu of the U_l term in the computation of the dimensionless numbers and the correlation is still of the form

$$\frac{\varepsilon_g}{\varepsilon_{go}} = C_o Re'^{a}_{lo} Fr'^{b}_{lo} We'^{c}_{lo} D^{*d} \text{ . (4.19)}$$

where, now

$$Re'_{lo} = \frac{j_l \delta_{MT}}{\nu_l}, \text{ (4.20)}$$

$$We'_{lo} = \frac{j_l^2 \delta_{MT} \rho_l}{g_c \sigma} \text{ (4.21)}$$

and

$$Fr'_{lo} = \frac{j_l^2}{g \delta_{MT}} \text{ . (4.22)}$$

Using numerical analysis for the optimization of the constants, the correlation becomes:

$$\frac{\varepsilon_g}{\varepsilon_{go}} = 1.30 \times 10^{-5} \left[Re'^{1.41}_{l} Fr'^{-0.420}_{l} We'^{-0.189}_{l} \right] \left(\frac{z}{\delta_{in}} \right)^{0.118} \text{ (4.23)}$$

with an R^2 fit of 0.95.

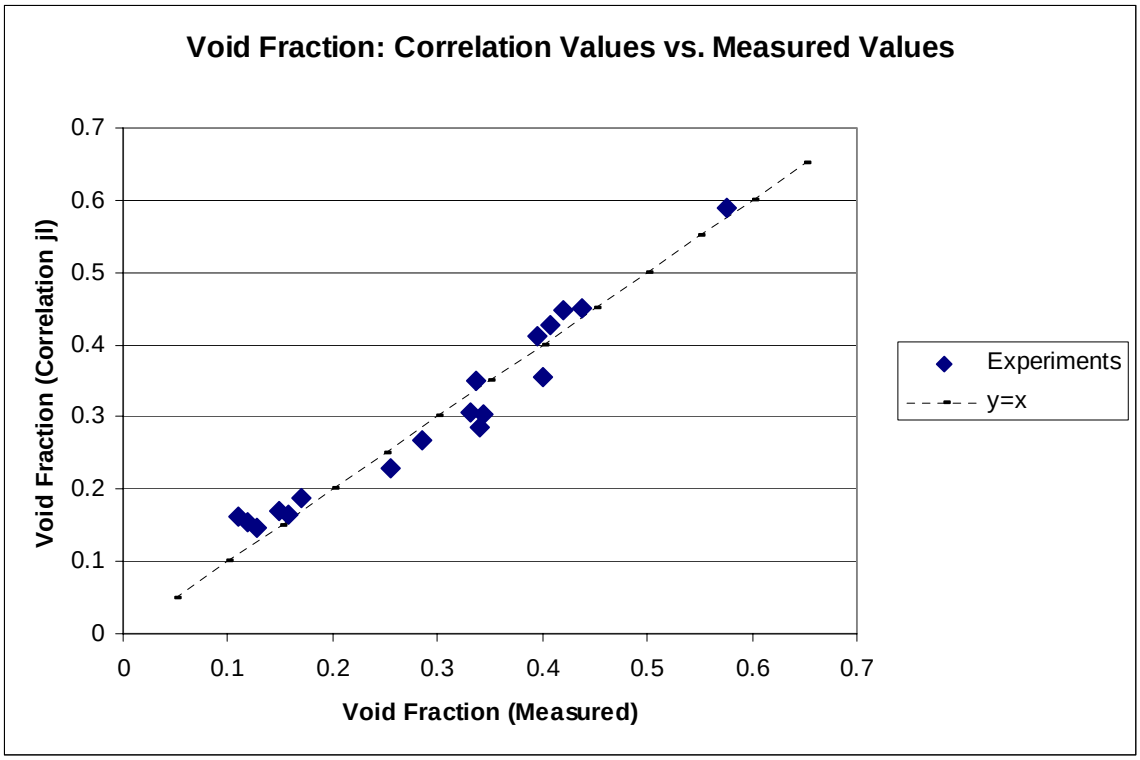

Figure 4.9: Measured void fraction versus correlation void fraction

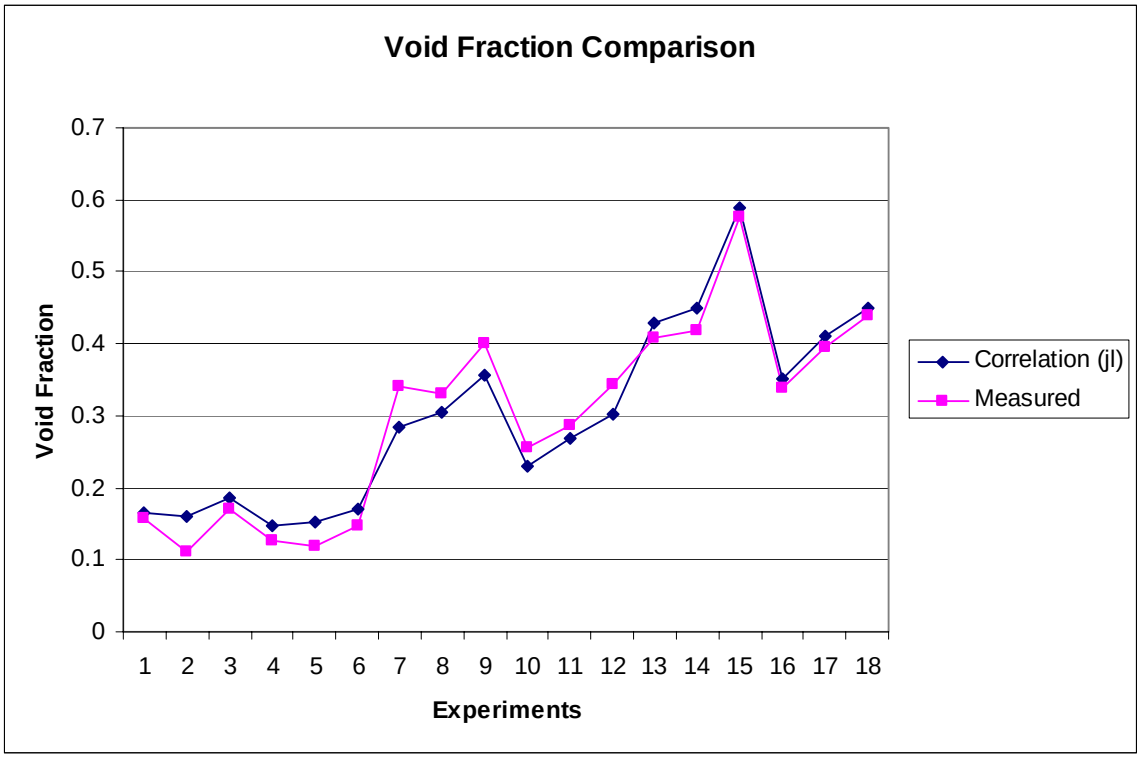

Figure 4.10: Void fraction comparison

A yet third type of correlation can be developed, and based on the generic form

$$\frac{\varepsilon_g}{\varepsilon_{go}} = C_o Re_{lo}^a Fr_{lo}^b We_{lo}^c D^{*d} \quad (4.24)$$

where

$$Re_{lo} = \frac{j_{lo}\delta_{in}}{\nu_l}, \quad (4.25)$$

$$We_{lo} = \frac{j_{lo}^2 \delta_{in} \rho_l}{g_c \sigma} \quad (4.26)$$

and

$$Fr_{lo} = \frac{j_{lo}^2}{g\delta_{in}}. \quad (4.27)$$

The advantage of this correlation is that it provides $\frac{\varepsilon_g}{\varepsilon_{go}}$ in terms of easily measurable parameters (i.e., δ_{MT} and w_{MT} are not used). The optimization of the coefficients in this correlation led to:

$$\frac{\varepsilon_g}{\varepsilon_{go}} = 1.58\times10^{-5}\left[Re_{lo}^{0.874}Fr_{lo}^{-0.252}We_{lo}^{0.306}\right]\left(\frac{z}{\delta_{in}}\right)^{0.180} \quad (4.28)$$

This correlation has an R^2 fit of 0.81, and the correlation values of the void fraction are compared to the measured values of the void fraction.

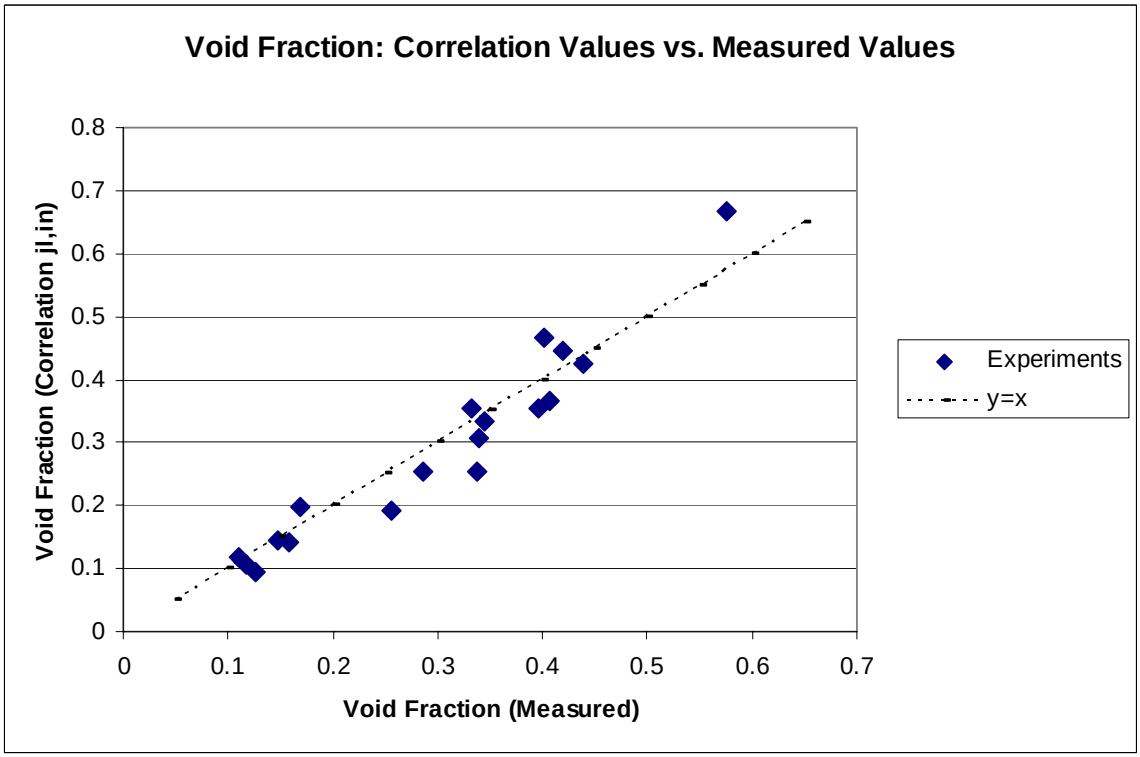

Figure 4.11: Measured void fraction versus correlation void fraction

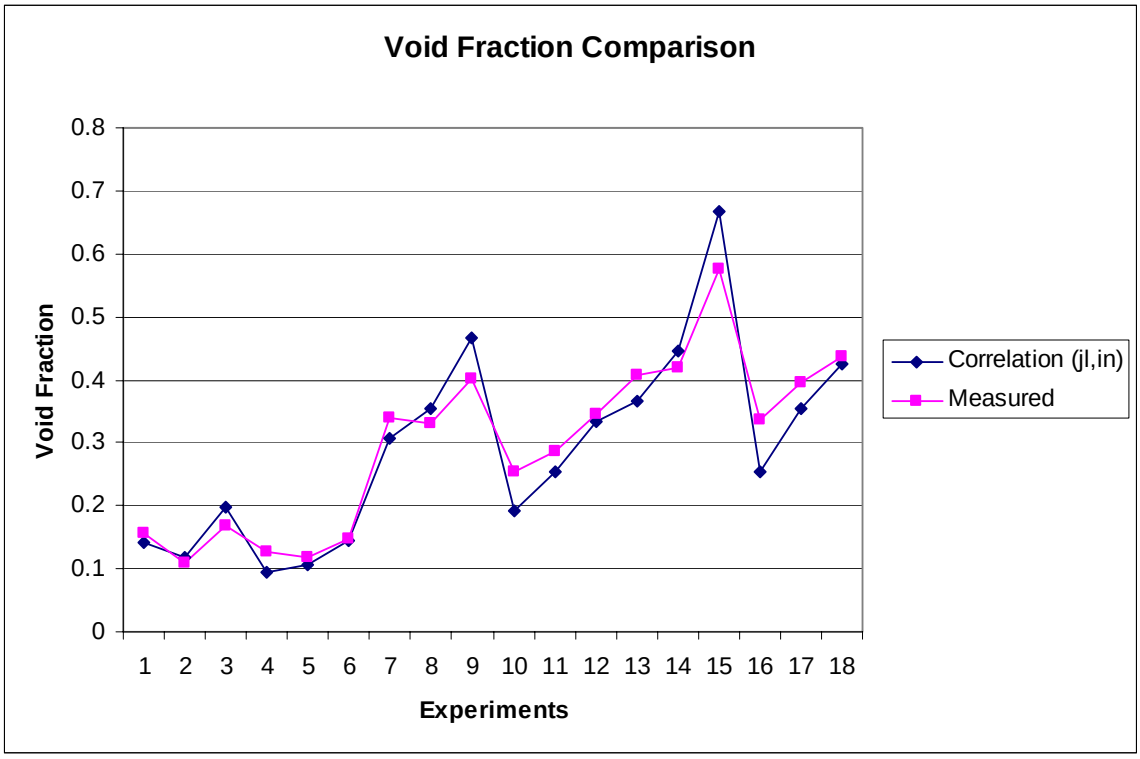

Figure 4.12: Void fraction comparison

IV.5. GAS FLOW LIMITS

Bubbly flow is the desired flow regime for the test flow. For each flow rate of water studied, the maximum gas flow for the bubbly flow regime was visually determined. For Q_l = 60 L/min (15.9 gpm), as gas is injected into the flow, the resulting flow regime is slug flow; therefore the maximum gas flow rate (Q_g / Q_l) is equal to 0. For Q_l = 120 L/min (31.7 gpm), bubble flow regime was observed for a maximum Q_g / Q_l of 1.25% (Q_g = 1.5 L/min). If the gas flow rate is increased, the resulting flow regime is slug flow. For Q_l = 180 L/min (47.6gpm), bubble flow regime was observed for a maximum Q_g / Q_l of 15% (Q_g = 27 L/min). At this value of Q_g, spray was observed

from the jet. Additional gas resulted in slug formation within the nozzle. For Q_l = 240 L/min (63.5 gpm), bubble flow regime was observed for a maximum Q_g / Q_l of 21% (Q_g = 50.5 L/min). Additional gas causes significant water spray since gas is escaping from the flow. And for Q_l = 288 L/min (76 gpm), bubble flow regime was observed for a maximum Q_g / Q_l of 21% (Q_g = 60.4 L/min). Additional gas causes significant water spray since gas is escaping from the flow.

CHAPTER V

CONCLUSIONS AND RECOMMENDATIONS

V.1. CONCLUSIONS

In this investigation, the hydrodynamics of falling two-phase jets were investigated. The jets were produced using a vertically-oriented, 10 cm x 1 cm rectangular nozzle and using air and water as the working fluids.

A total of 20 different flow rates were studied and local measurements were performed at nine locations for each flow rate covering the z-dimension range from 5.4 cm to 21.9 cm at the nozzle exit. The collapsed liquid thickness was measured for all points using a gamma-ray densitometer, and the jet thickness was measured using a thickness tester. The void fraction was then calculated for all data points. However, due to the relatively large error associated with the jet thickness measurements as well as the potential “jet spray”, the data representing low liquid flow rates were excluded, and the void fraction was empirically correlated for only the six, highest velocity tests. The local gas phase and liquid phase velocities as well as the slip ratios were also studied for the six flow rates. The limits for jet stability were qualitatively assessed.

V.1.1 Void Fraction

The trends in the void fraction of the aforementioned six flow rates were studied in some detail. The void fractions ranged from below 10% to almost 60%. In all cases, however, the void fraction was greater than the volumetric flow rate ratio. Generally as the distance from the nozzle increased, the void fraction increased. Three different correlations were developed, all using inlet flow conditions and jet exit thickness, as well as two using local thickness and width measurements. The distinction between them is the definition of a velocity used in the calculation of the dimensionless numbers used in the respective correlations; the first used a localized velocity with dependence on the local void fraction and local thickness, the second used a superficial velocity and local thickness, and the third used the superficial velocity and jet thickness at nozzle exit. All three correlations fitted the data well.

V.1.2. Velocity Slip

The slip ratio of six different flow rates was extensively studied. The values of the slip ratio ranged from less than 0.2 to greater than 0.8. Thus, at no positions studied was the gas velocity greater than the liquid velocity. This suggests that the homogeneous equilibrium model is inappropriate (since the assumption that the slip ratio is equal to 1 is clearly invalid). Generally as the distance from the nozzle increased, the slip ratio decreased, indicting the liquid is accelerating and or the gas is decelerating. The deceleration of the gas is of course expected, due to the buoyancy effect.

V.1.3. Gas Flow Limits

The stability limits were studied for five different water flow rates. In the context of the present experiments, jet stability is primarily determined by the two-phase flow regime upstream the exit from the nozzle. The bubbly flow regime was required for the formation of a stable jet. It was observed that, when the water flow rate was small (60 L/min [15.9 gpm], 120 L/min [31.7 gpm]), the flow became slug flow almost immediately with any gas injection. For higher water flow rates (240 L/min [63.5 gpm], 288 L/min [76 gpm]), the flow became unstable only after a substantial amount of gas was added ($Q_g / Q_l > 20\%$).

V.2. RECOMMENDATIONS

Further study of plane two-phase falling jets with the current test facility is recommended. There are several different facets that can be elaborated. First, the number of experimental data points can be increased by studying higher water flow rates (greater than 288 L/min [76 gpm]), and by increasing the number of positions where measurements are performed for each flow rate.

As previously discussed , at low gas flow rates, the thickness measurements are slightly underpredicted and the collapsed liquid thickness values have been slightly overpredicted. It is not completely clear why this anomaly occurs, and whether the anomaly is physical or it is caused by experimental errors. If the latter possibility is to be believed, then the method used to measure the thickness of the jet is not accurate enough

for when trying to measure small void fractions (less than 10%). Further investigation of this anomaly is recommended. Another means of measurement for the jet thickness (photography, etc.) is recommended. The spray from the jet that deposits onto the container walls can possibly be estimated by normalizing the void fraction of single phase flow to 0% (if a negative value is observed due to the spray).

The measurements in this study were restricted to a minimum distance from the nozzle exit of 5.4 cm and a maximum distance from the nozzle exit of 21.9 cm. It is recommended that the facility be modified so that measurements at larger distances from the nozzle exit become feasible.

Finally, the stability of liquid jets when bubbles are generated inside the falling jet (due to flashing caused by volumetric heating for example) should be investigated in the future.

APPENDIX A

UNCERTAINTY ANALYSIS

A.1. Gamma-Ray Densitometer

Experiments with goals to determine an appropriate counting time for the gamma-ray densitometer were conducted. The error associated with the void fraction is

$$\frac{\Delta\alpha}{\alpha} = \frac{1}{\sqrt{I_{2\phi} n}} \frac{\left[2\left(1-\alpha+\alpha^2\right)\right]^{1/2}}{\alpha \ln\left(I_g / I_l\right)} \quad \text{(A.1)}$$

where n is the number of times the experiment has been repeated (Lindsay et al., 1995). In addition, the counts for each respective phase will increase as the counting time increases. A counting time of five minutes with three repetitions was proposed. Using the average of the three trials for $I_{2\phi}$, the average error was approximately 0.62% (repeatability). It is also important to compare the values of $I_{2\phi}$ for each of the trial runs. Five experiments were conducted and for each experiment, all nine positions were tested three times. The average value of the standard deviation divided by the average $\left\langle \sigma / \overline{x} \right\rangle$ was only 0.487%. Therefore, the variance from trial to trial for a given flow rate at a fixed position is low. It was then decided that the number of trials can be reduced to one since the five minute counting time is sufficiently large. This would then increase the error associated with the void fraction by a factor of $\sqrt{3}$, nonetheless, the error is still acceptable.

The error associated with the calibration of the densitometer was also assessed. Ten, five minute counts were taken with the empty container as well as the container filled with water. The values of $\langle \sigma / \overline{x} \rangle$ for the empty container and the water-filled container were 0.171% and 0.522% respectively. This deviation is very small so only one calibration is needed per time period.

A.2. Jet Thickness and Width Measurements

The error associated with the jet thickness tester was also studied. All 20 different flows were measured at all nine locations, and the thicknesses were recorded. The experiments were then repeated, and the thicknesses were compared from the first trial to the second. Overall the discrepancies were small (average difference of 1.3%). The "trouble spots" that were identified were then studied further. Ten experiments were run for these trouble spots to gather a more accurate value of the standard deviation of these measurements so appropriate error bars could be formed. The values of $\langle \sigma / \overline{x} \rangle$ were assessed, and typically were in the range of 1.0 - 1.5%. The void fraction versus distance from the nozzle is plotted in Figure A.1 using all the measured thickness values for the associated flow rates so the total uncertainty bands associated with repeatability could be shown.

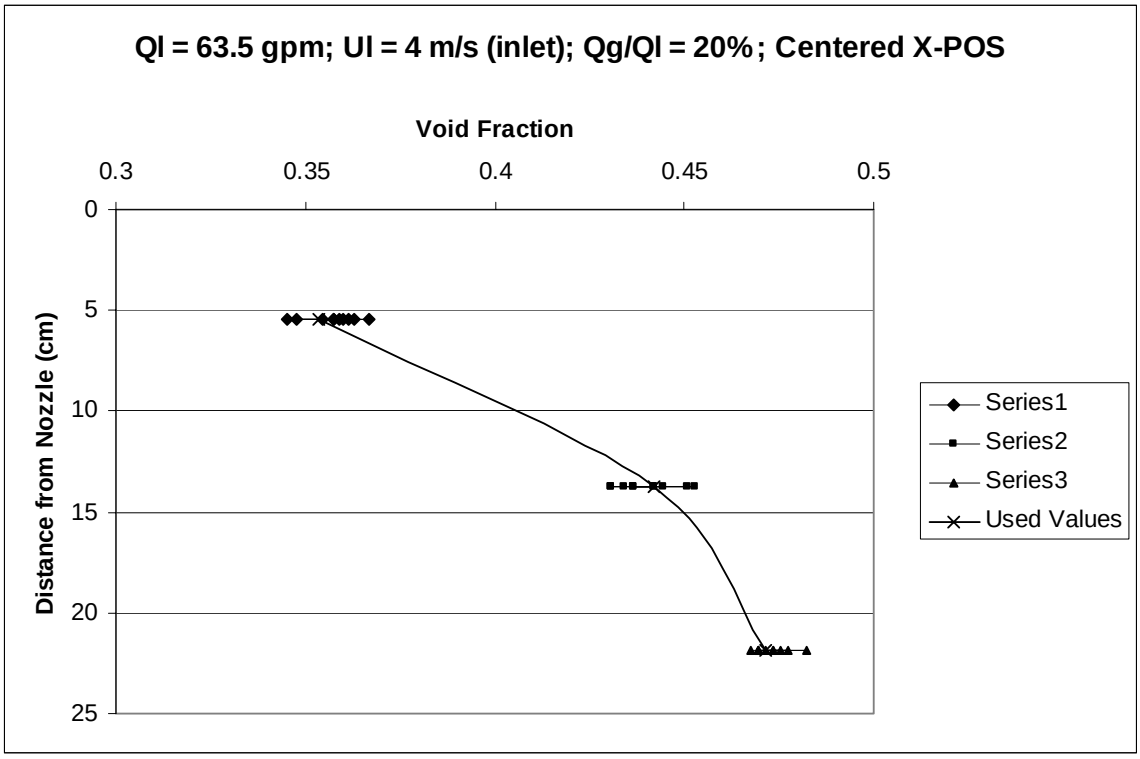

Figure A.1: Void fraction versus distance from the nozzle (with error bars)

The error associated with the jet width measurement was also assessed. Two photographs were taken for each flow rate at different zooms, and the on-screen software ruler was used to calibrate each photo. The average deviation of jet width among the two photographs was only 1.57%.

APPENDIX B

CORRELATION COMPARISONS

The three empirical correlations for void fraction from section IV.4. are now compared. As noted previously, these correlations differed from one another with respect to the velocity term (local or superficial) and thickness term (local or nozzle exit). The first two correlations fit the data remarkably well as they both have an R^2 fit of 0.95. The similarity between these two correlations was the use of the local measured thickness in the calculation of Reynolds, Froude and Weber numbers. The third correlation used nozzle exit values, and it did not fit the data as well as the correlations using local values. It has an R^2 fit of 0.81. Figures B.1, B.2 and B.3 are comparisons of the aforementioned correlations. The correlations are referenced by their respective characteristic velocity term (U_l , j_l and $j_{l,in}$).

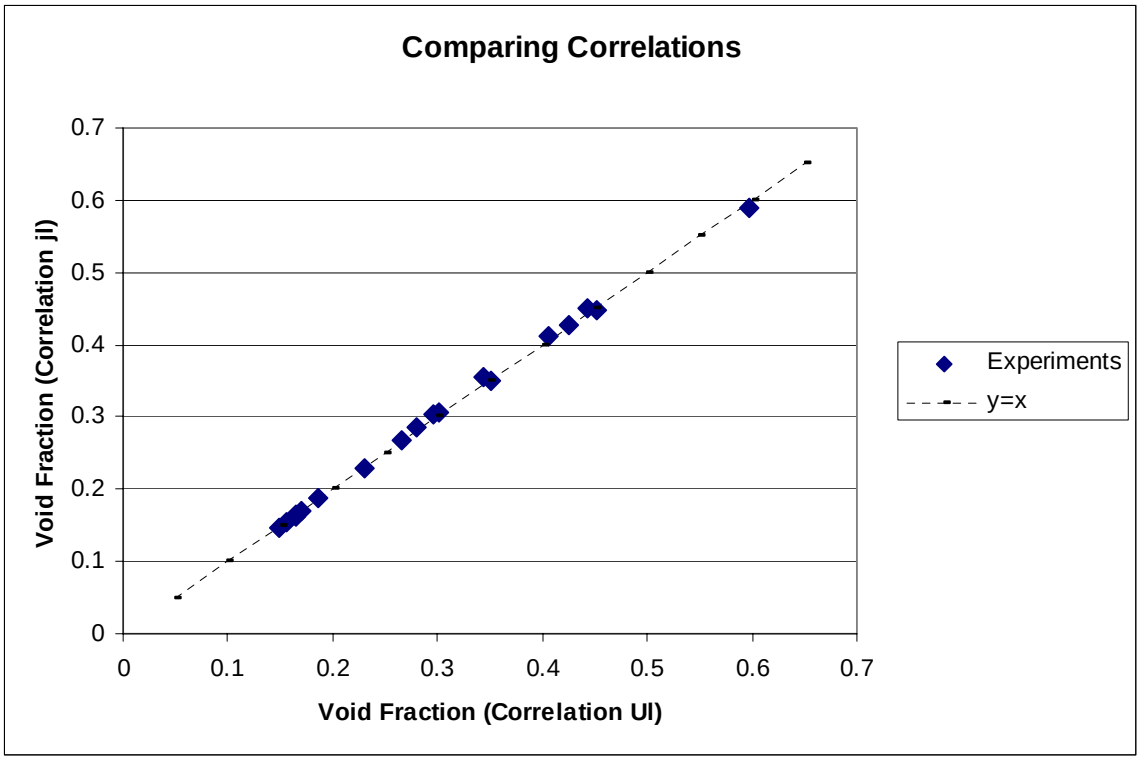

Figure B.1: Comparing correlations (j_l vs. U_l)

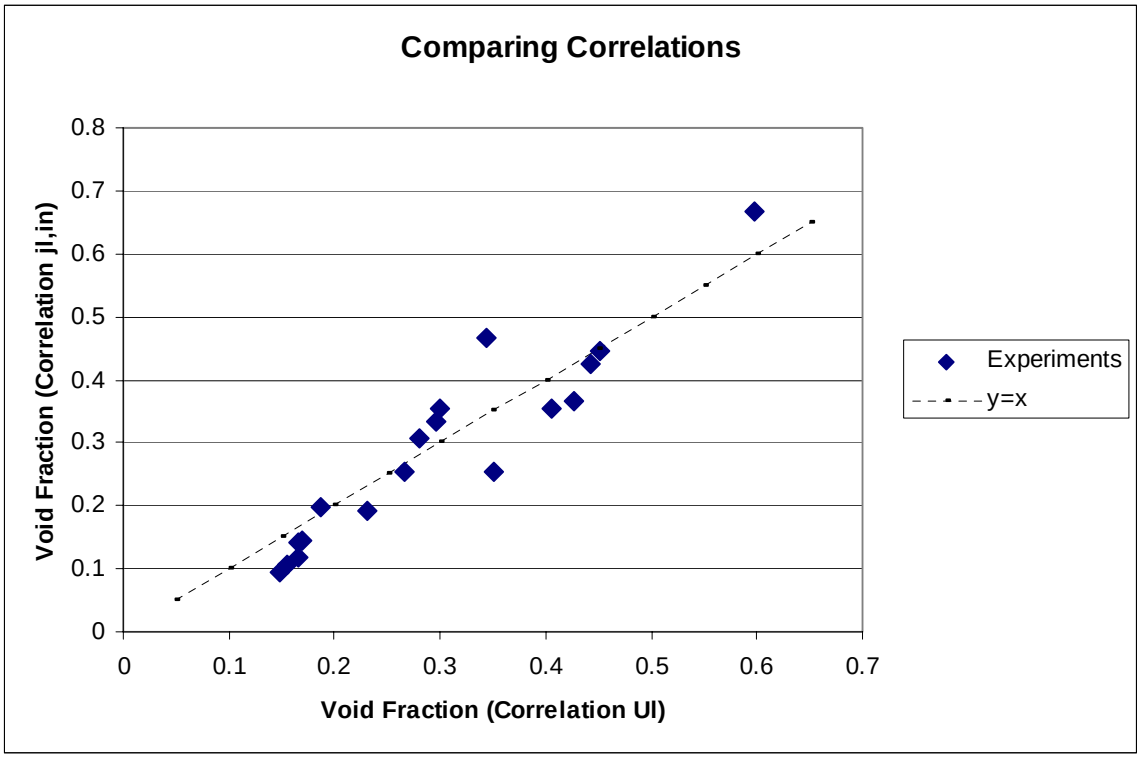

Figure B.2: Comparing correlations ($j_{l,in}$ vs. U_l)

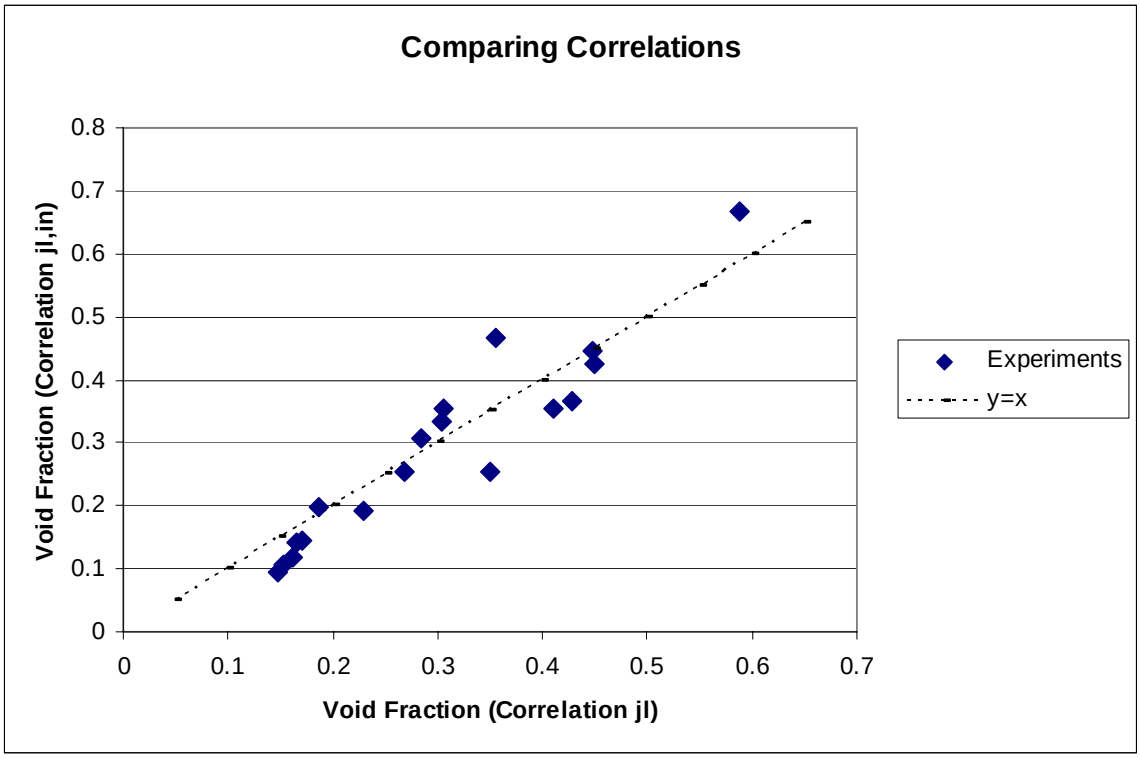

Figure B.3: Comparing correlations ($j_{l,in}$ vs. j_l)

APPENDIX C

DATA TABLES

The positions used in the data tables are defined as the following:

Table C.1 Positions defined

Position	x-position (cm)	z-position (cm)
1	-1.42875	5.4
2	0	5.4
3	1.42875	5.4
4	-1.42875	13.7
5	0	13.7
6	1.42875	13.7
7	-1.42875	21.9
8	0	21.9
9	1.42875	21.9

The x-position is relative to the centerline of the jet, and the z-position is the distance from the nozzle (see Figure 3.5).

All the count measurements were taken for a five minute counting interval. The volumetric water flow rate is defined in terms of the initial water jet velocity.

Table C.2 Count values for single phase flow (Q_g / Q_l = 0%)

Position	4.79 m/s	4 m/s	3 m/s	2 m/s	1 m/s
1	6,489,231	6,498,198	6,519,360	6,588,725	6,733,789
2	6,500,558	6,509,992	6,529,202	6,600,823	6,775,716
3	6,507,652	6,519,339	6,546,963	6,620,459	6,791,502
4	6,571,918	6,604,925	6,646,792	6,766,576	7,011,256

Table C.2 (Continued)

5	6,563,425	6,589,736	6,645,253	6,761,546	6,988,362
6	6,561,749	6,574,267	6,628,018	6,756,107	6,994,371
7	6,605,559	6,625,202	6,690,975	6,819,129	7,098,507
8	6,538,550	6,571,741	6,649,452	6,820,676	7,064,453
9	6,570,276	6,601,075	6,662,476	6,823,910	7,078,371

Table C.3 Count values for two-phase flow
(Q_g / Q_l = 2.5% and 1.25% for the 2 m/s flow)

Position	4.79 m/s	4 m/s	3 m/s	2 m/s
1	6,540,575	6,545,826	6,580,542	6,616,108
2	6,555,655	6,559,432	6,586,160	6,634,886
3	6,566,674	6,577,539	6,600,943	6,659,613
4	6,611,719	6,625,448	6,684,794	6,800,279
5	6,608,847	6,620,842	6,677,224	6,791,810
6	6,592,780	6,605,945	6,642,311	6,797,030
7	6,634,957	6,645,371	6,714,555	6,854,342
8	6,561,880	6,596,293	6,679,247	6,855,388
9	6,598,998	6,628,326	6,683,571	6,875,844

Table C.4 Count values for two-phase flow (Q_g / Q_l = 5%)

Position	4.79 m/s	4 m/s	3 m/s
1	6,530,931	6,535,530	6,558,472
2	6,541,888	6,544,717	6,574,183
3	6,552,619	6,558,818	6,583,053
4	6,613,365	6,626,113	6,670,716
5	6,600,762	6,618,355	6,660,059
6	6,575,921	6,586,913	6,625,337
7	6,588,797	6,634,779	6,701,000
8	6,544,354	6,576,338	6,663,653
9	6,580,544	6,610,453	6,667,295

Table C.5 Count values for two-phase flow (Q_g / Q_l = 10%)

Position	4.79 m/s	4 m/s	3 m/s
1	6,624,483	6,633,217	6,661,813
2	6,633,190	6,647,182	6,668,481
3	6,638,856	6,652,563	6,672,338
4	6,658,372	6,665,099	6,700,546
5	6,678,892	6,684,946	6,704,142
6	6,661,094	6,688,203	6,702,553
7	6,675,861	6,681,913	6,706,380
8	6,659,027	6,672,994	6,684,886
9	6,675,134	6,706,136	6,712,834

Table C.6 Count values for two-phase flow (Q_g / Q_l = 15%)

Position	4.79 m/s	4 m/s	3 m/s
1	6,720,074	6,725,203	6,700,265
2	6,741,821	6,742,937	6,713,866
3	6,742,691	6,750,579	6,725,722
4	6,686,782	6,676,654	6,703,489
5	6,757,850	6,762,688	6,740,092
6	6,785,448	6,798,654	6,762,274
7	6,735,724	6,728,745	6,750,147
8	6,807,341	6,800,109	6,733,425
9	6,803,821	6,813,211	6,774,724

Table C.7 Count values for two-phase flow (Q_g / Q_l = 20%)

Position	4.79 m/s	4 m/s
1	6,643,090	6,646,962
2	6,724,173	6,721,756
3	6,750,433	6,747,303
4	6,694,991	6,691,049
5	6,779,880	6,787,176
6	6,795,533	6,781,186
7	6,769,755	6,786,458
8	6,784,279	6,790,212

Table C.7 (Continued)

9	6,793,896	6,803,376

Table C.8 Calibration count values for the experiments

Q_g / Q_l	I_l	I_g
0, 5, 10 & 15%		
	2,779,912	7,629,748
	2,774,633	7,642,454
2.5 & 1.25%		
	2,774,698	7,663,588
	2,771,274	7,669,410
20%		
	2,776,710	7,607,864
	2,771,136	7,596,290

The differing values of Q_g / Q_l correspond to separate days where experiments were conducted. The two values for each day correspond to the values at the beginning and end of the each experiment day, and the average of these values were used in the container void fraction calculations.

Table C.9 Jet thickness values (inch x 10^3)

Day 1						
U_l (m/s); Q_g / Q_l (%)	1a	2a	3a	1b	2b	3b
4.79;0	492	493	495	622	622	623
4;0	485	487	480	619	620	617
3;0	481	481	480	620	621	621
2;0	462	461	462	618	620	619
1;0	424	418	431	611	617	605
4.79;2.5	481	469	468	642	638	641
4;2.5	480	471	457	622	618	630

Table C.9 (Continued)

3;2.5	470	450	458	610	610	620
2;1.25	460	446	445	606	601	605
4.79;5	484	477	493	631	627	626
4;5	475	458	462	619	624	625
3;5	474	457	459	611	613	618
4.79;10	501	480	475	650	658	655
4;10	492	480	480	624	635	640
3;10	495	473	473	614	625	629
4.79;15	520	540	537	660	673	676
4;15	502	506	490	638	636	642
3;15	500	484	471	631	643	642
U_l (m/s); Q_g / Q_l (%)	4a	5a	6a	4b	5b	6b
4.79;0	565	538	540	540	551	551
4;0	550	535	534	540	548	547
3;0	499	498	500	571	574	572
2;0	483	463	476	542	555	550
1;0	409	416	394	538	530	560
4.79;2.5	553	541	540	563	565	570
4;2.5	558	531	540	542	569	570
3;2.5	540	528	523	542	555	570
2;1.25	487	466	465	553	558	565
4.79;5	570	555	548	550	550	556
4;5	550	529	529	561	561	556
3;5	535	508	528	556	556	560
4.79;10	575	542	539	542	546	557
4;10	567	540	550	537	545	560
3;10	550	518	510	525	542	551
4.79;15	613	595	581	592	595	590
4;15	591	581	555	571	584	591
3;15	573	568	529	535	563	591
U_l (m/s); Q_g / Q_l (%)	7a	8a	9a	7b	8b	9b
4.79;0	621	607	601	475	490	502
4;0	605	592	595	480	490	490
3;0	545	551	550	510	520	517
2;0	503	492	470	507	522	532
1;0	394	353	366	520	565	544
4.79;2.5	609	615	630	462	481	504
4;2.5	585	600	599	476	479	488
3;2.5	550	550	575	513	504	504

Table C.9 (Continued)

2;1.25	510	495	479	495	497	501
4.79;5	625	607	600	525	522	518
4;5	618	600	587	480	497	511
3;5	583	571	560	500	503	508
4.79;10	642	637	590	497	504	525
4;10	620	606	581	512	510	510
3;10	602	607	562	490	514	504
4.79;15	681	670	640	545	570	565
4;15	651	641	599	523	570	550
3;15	621	626	591	513	538	510
Day 2						
U_l (m/s); Q_g / Q_l (%)	1a	2a	3a	1b	2b	3b
4.79;0	520	515	509	597	602	604
4;0	518	509	502	588	600	608
3;0	513	497	497	588	597	596
2;0	495	488	477	585	585	591
1;0	471	466	451	567	570	571
4.79;2.5	530	513	526	592	590	577
4;2.5	518	495	497	586	597	583
3;2.5	505	480	488	582	585	590
2;1.25	493	474	468	579	582	595
4.79;5	537	520	514	588	590	605
4;5	522	508	493	575	577	600
3;5	521	482	493	570	590	581
4.79;10	555	537	540	592	604	597
4;10	533	521	522	593	602	603
3;10	530	494	495	585	609	610
4.79;15	579	588	577	604	611	622
4;15	555	543	529	591	607	610
3;15	530	541	522	605	594	597
U_l (m/s); Q_g / Q_l (%)	4a	5a	6a	4b	5b	6b
4.79;0	575	554	548	529	534	540
4;0	558	547	540	542	543	555
3;0	542	532	524	530	542	545
2;0	491	480	486	537	540	533
1;0	410	402	404	530	542	547
4.79;2.5	567	557	564	555	554	541
4;2.5	558	547	551	543	555	552

Table C.9 (Continued)

3;2.5	534	534	525	551	541	553
2;1.25	487	472	466	555	555	563
4.79;5	576	554	559	548	552	543
4;5	562	533	543	553	555	555
3;5	539	508	518	559	565	562
4.79;10	585	565	549	540	530	559
4;10	561	546	552	552	540	565
3;10	559	549	566	522	522	508
4.79;15	611	602	580	594	582	585
4;15	603	597	584	557	557	563
3;15	551	559	553	555	575	570
U_l (m/s); Q_g / Q_l (%)	7a	8a	9a	7b	8b	9b
4.79;0	585	565	553	518	533	541
4;0	565	558	541	523	527	540
3;0	542	558	554	521	522	513
2;0	496	497	491	515	510	515
1;0	381	371	374	518	538	537
4.79;2.5	578	597	622	497	499	505
4;2.5	561	573	570	507	511	522
3;2.5	561	548	555	508	512	510
2;1.25	508	489	462	499	505	521
4.79;5	640	622	597	497	499	525
4;5	601	589	584	494	496	500
3;5	570	541	540	511	530	530
4.79;10	659	621	606	487	507	505
4;10	622	612	577	505	504	517
3;10	581	588	546	505	525	522
4.79;15	672	681	663	540	537	536
4;15	660	642	600	520	549	548
3;15	666	660	616	470	490	495
Day 3						
U_l (m/s); Q_g / Q_l (%)	1a	2a	3a	1b	2b	3b
4.79;20	642	630	608	626	625	618
4;20	598	591	555	610	606	624
U_l (m/s); Q_g / Q_l (%)	4a	5a	6a	4b	5b	6b
4.79;20	627	631	622	610	600	595

Table C.9 (Continued)

4;20	621	630	606	584	599	594
U_l (m/s); Q_g / Q_l (%)	7a	8a	9a	7b	8b	9b
4.79;20	712	709	655	601	638	610
4;20	648	681	644	550	574	571
U_l (m/s); Q_g / Q_l (%)	1a	2a	3a	1b	2b	3b
4.79;20	637	628	611	627	626	622
4;20	594	593	560	609	607	631
U_l (m/s); Q_g / Q_l (%)	4a	5a	6a	4b	5b	6b
4.79;20	631	634	621	608	594	595
4;20	623	633	608	585	590	588
U_l (m/s); Q_g / Q_l (%)	7a	8a	9a	7b	8b	9b
4.79;20	707	706	658	603	639	615
4;20	650	680	643	551	572	572

The values of the jet thickness were taken on several days and compared to get an estimate on the error associated with the thickness measurements. For each position, the "a" and "b" values were measured from each side of the jet (see Figure 3.12).

Table C.10 Jet thickness tester calibration values (inch x 10^3)

	1a	2a	3a	1b	2b	3b
Day 1	306	314	335	421	415	395
Day 2	314	313	327	410	412	400
Day 3	310	313	333	414	413	394

The three values for each position were averaged in the calculation of jet thickness.

Table C.11 Jet thickness measurements used for the error analysis (U_l = 2 m/s; Q_g / Q_l = 1.25%)

1a	2a	3a	1b	2b	3b
497	495	488	599	597	590
497	486	493	593	597	603
502	488	478	593	597	594
503	488	489	590	588	594
505	489	483	594	588	595
499	482	480	579	586	591
499	487	475	580	590	588
502	489	481	585	591	590
499	488	479	583	586	596
500	487	479	590	593	589

Table C.12 Jet thickness measurements used for the error analysis (U_l = 3 m/s; Q_g / Q_l = 15%)

4a	5a	6a	4b	5b	6b
628	640	602	561	602	597
602	642	602	585	610	583
595	626	583	572	608	569
608	624	584	564	597	572
620	645	606	568	597	585
611	635	592	569	599	577
604	640	601	574	602	580
617	629	599	572	595	582
609	642	607	570	600	579
610	640	593	580	599	578

Table C.13 Jet thickness measurements used for the error analysis (U_l = 4.79 m/s; Q_g / Q_l = 0%)

7a	8a	9a	7b	8b	9b
601	612	601	472	476	499
599	613	617	471	473	496
621	607	608	488	474	500
624	608	595	486	473	495
617	599	603	477	478	500
611	610	606	481	478	499

Table C.13 (Continued)

602	606	604	484	477	492
620	599	599	479	481	504
617	607	599	477	477	499
613	601	602	480	478	503

Table C.14 Jet width measurements (cm) U_l **= 4 m/s**

Distance from		Q_g / Q_l	
Nozzle (cm)	10%	15%	20%
5.4	10.65079365	10.529695	10.5362587
13.7	10.80952381	10.5617978	10.6594414
21.9	10.47619048	10.4333868	10.6011102

Table C.15 Jet width measurements (cm) U_l **= 4.79 m/s**

Distance from		Q_g / Q_l	
Nozzle (cm)	10%	15%	20%
5.4	10.55968326	10.5922131	10.2699516
13.7	10.62553772	10.8937086	10.4712746
21.9	10.49449797	10.5139563	10.2347654

BIBLIOGRAPHY

Atkinson, B.W., Jameson, G.J., Nguyen, A.V., Evans, G.M., and Machniewski, P.M., 2003, "Bubble breakup and coalescence in a plunging liquid jet bubble column," *Canadian J. Chem. Eng.*, vol. 81, n. 3-4, pp. 519-527.

Cicchitti, A., Lombardi, C., Silvestri, M., Soldaini, G., and Zavattarelli, R., 1960, "Two-phase cooling experiments – pressure drop, heat transfer and burnout measurements," *Energia Nucleare*, vol. 7, pp. 407-425.

Clift, R., Grace, J.R. and Weber, M.E., 1978, *Bubbles Drops and Particles*, Academic Press, New York.

Collier, J.G., and Thome, J.R., 1994, *Convective Boiling and Condensation*, Oxford University Press.

Collier, J.G., and Thome, J.R., 1996, *Convective Boiling and Condensation*, 3rd Ed., Oxford University Press, U.K., pp. 10-90.

Davidson, J.R., and Harrison, D., 1971, *Fluidization*, Academic Press, New York.

Dukler, A.E., Wicks, M., and Cleveland, R.G., 1964, "Pressure drop and hold-up in two-phase flow part A – A comparison of existing correlations" and "Part B – An approach through similarity analysis," *AIChE Journal*, vol. 10, pp. 38-51.

Durst, F., and Zare, M., 1975, "Laser Doppler measurements in two-phase flows", *Proceedings of the I.D.A. Symposium*, Copenhagen, Denmark, pp. 403-429.

Durst, F., Melling, A., and Whitelaw, J.H., 1976, *Principles and Practice of Laser-Doppler Anemometry*, Academic Press, London.

Evans, G.M., Jameson G.J., and Atkinson, B.W., 1992, "Prediction of the bubble size generated by a plunging liquid jet bubble column," *Chem. Eng. Sci.*, vol. 47, pp. 3265-3272.

Evans, G.M. and Jameson G.J., 1995, "Hydrodynamics of a plunging liquid jet bubble column," *Transactions of the Institute of Chem. Eng.*, vol. 73, pp. 679-684.

Hewitt, G.F., and Roberts, D.N., 1969, "Studies of two-phase flow patterns by simultaneous x-ray and flash photography," AERE-M 2159, HNSO.

Hinze, J.O., 1975, *Turbulence – An Introduction to its Mechanism and Theory*, McGraw-Hill, New York, NY.

Ishii, M., and Mishima, K., 1984, “Two-fluid model and hydrodynamic constitutive relations,” *Nuclear Engineering Design*, vol. 82, pp. 107-126.

Kuboi, R., Komosawa, I., and Otake, T., 1972, “Collision and coalescence of dispersed drops in turbulent liquid flow,” *J. Chem Eng Japan*, vol. 5, pp. 423-424.

Kumar, S., Nikitopoulos, D.N., and Michaelides, E.E, 1989, “Effect of bubbles on the turbulence near the exit of a liquid jet,” *Experiments in Fluids*, vol 7, pp. 487-494.

Lahey, R.T. Jr., and Moody, F.J., 1993, *The Thermal Hydraulics of a Boiling Water Nuclear Reactor*, 2nd Ed., *American Nuclear Society*, LaGrange Park, Illinois.

Lindsay, J.D., Ghiaasiaan S.M., and Abdel-Khalik, S.I., 1995, “Macroscopic flow structures in a bubbling paper pulp-water slurry,” *Ind. Eng. Chem. Research*, vol. 34, n. 10, pp. 3342-3354.

McAdams, W.H., Woods, W.K., and Bryan, R.L., 1942, “Vaporization inside horizontal tubes – II – Benzene-oil mixtures,” *Trans. ASME*, vol. 64, pp. 193.

Morel, T., 1975, “Comprehensive design of axisymmetric wind tunnel contractions,” *J. Fluids Eng.*, pp. 225-233.

Nicklin, D.J., Wilkes, J.O., and Wilkes, J.F., 1962, “Two-phase flow in vertical tubes,” *Trans. Inst. Chem. Eng.*, pp. 40-61.

Ohkawa, A., Shiokawa, Y., Sakai, N., and Imai, H., 1985, “Flow characteristics of downflow bubble columns with gas entrainment by a liquid jet,” *J. Chem. Eng. Japan*, vol. 18, n. 5, pp. 466-469.

Stahl, P., and von Rohr, P.R., 2004, "On the accuracy of void fraction measurements by single beam gamma-densitometer for gas-liquid two-phase flows in pipes,” *Experimental Thermal and Fluid Science*, vol. 28, n. 6, pp. 533-544.

Stanley, K.N., and Nikitopoulos, D.E., 1996, “Bubble measurements in a gas liquid jet,” *Chem. Eng. Communications*, vol. 143, pp. 1-22.

Vince, M.A., and Fincke, J.R., 1983, “The relationship between density and void fraction measurement uncertainty in radiation densitometry,” *Int. J. Multiphase Flow*, vol. 9, no. 4, pp. 447-449.

Wallis, G.B., 1962, “A simplified one-dimensional representation of two-component vertical flow and its application to batch sedimentation,” *Symp Interaction Between Fluids and Particles* (*IChemE*, London), pp. 9-16.

Wallis, G.B., 1969, *One-Dimensional Two-Phase Flow*, McGraw-Hill, New York.

Yamagiwa, K., Kusabiraki, D., and Ohkawa, A., 1990, “Gas holdup and gas entrainment rate in downflow bubble column with gas entrainment by a liquid jet operating at high liquid throughput,” *J. of Chem. Eng. of Japan*, vol. 23, n. 3, pp. 343-348.

Zuber, N., and Findlay, J.A., 1965, “Average volume concentration in two-phase flow systems,” *J. Heat Transfer*, series C, 453-468.

Zuber, N., Staub, F.W., Bijwaard, G., and Kroeger, P.G., 1967, “Steady state and transient void fraction in two-phase flow systems,” GEAP 5417.